Hall, I.R., Hemming, S.R., LeVay, L.J., and the Expedition 361 Scientists Proceedings of the International Ocean Discovery Program Volume 361 publications.iodp.org



doi:10.14379/iodp.proc.361.106.2017

Site U1477¹



I.R. Hall, S.R. Hemming, L.J. LeVay, S. Barker, M.A. Berke, L. Brentegani, T. Caley, A. Cartagena-Sierra, C.D. Charles, J.J. Coenen, J.G. Crespin, A.M. Franzese, J. Gruetzner, X. Han, S.K.V. Hines, F.J. Jimenez Espejo, J. Just, A. Koutsodendris, K. Kubota, N. Lathika, R.D. Norris, T. Periera dos Santos, R. Robinson, J.M. Rolinson, M.H. Simon, D. Tangunan, J.J.L. van der Lubbe, M. Yamane, and H. Zhang²

Keywords: International Ocean Discovery Program, IODP, JOIDES Resolution, Expedition 361, Site U1477, Agulhas Current, Agulhas Leakage, Agulhas Plateau, Agulhas Retroflection, Agulhas Return Current, Agulhas Rings, Agulhas Undercurrent, Atlantic Meridional Overturning Circulation, boundary current, Cape Basin, Circumpolar Deep Water, Congo Air Boundary, Delagoa Bight, East Madagascar Current, human evolution, Indian Ocean, Indonesian Throughflow, interocean exchange, Intertropical Convergence Zone, Last Glacial Maximum, Limpopo River, Middle Pleistocene Transition, Miocene, Mozambique Channel, Natal Valley, North Atlantic Deep Water, ocean circulation, paleoceanography, paleoclimate, Pleistocene, Pliocene, salinity, southern Africa, Southern Ocean, Subantarctic Zone, Subtropical Front, Subtropical Gyre, thermohaline circulation, Warm Water Route, Western Boundary Current, Zambezi River

Contents

- Background and objectives
- 4 Operations
- **6** Sedimentology
- **11** Physical properties
- 13 Micropaleontology
- 16 Paleomagnetism
- 18 Stratigraphic correlation
- 20 Geochemistry
- 23 Age model
- 23 References

Background and objectives

Site U1477 is located in the western Mozambique Channel on the upper continental slope (19°21.29'S; 36°54.90'E), ~65 nmi east of the Zambezi River delta region, at a water depth of 429.2 m below sea level (mbsl) (Figures F1, F2).

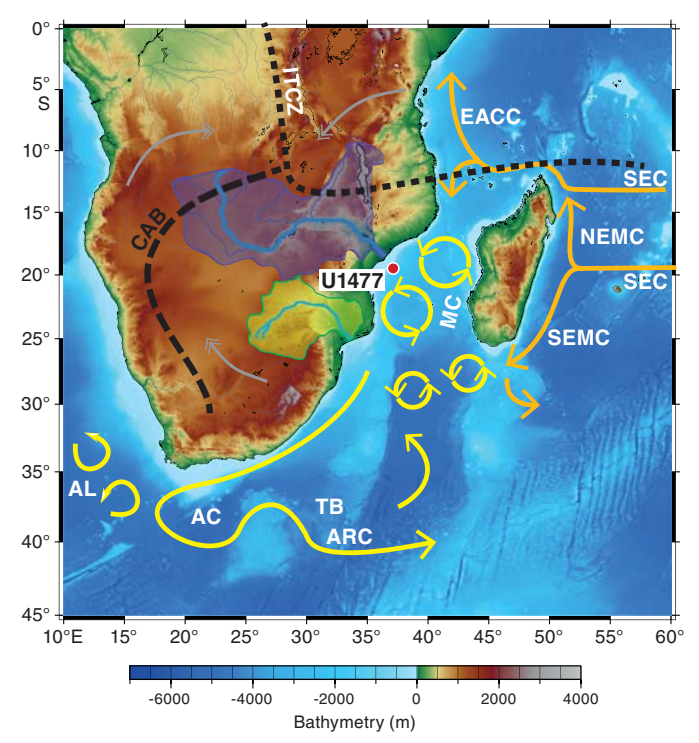
Site U1477 receives fluvial material exported from the Zambezi River basin catchment (Figures F1, F2), which is situated in the southernmost reach of the African monsoonal precipitation belt and drains multiple subbasins with differing basement lithologies, soils, and vegetation assemblages. Collectively, these subbasins span ~1.385 million km², and the river itself extends over 2500 km. Originating in northern Zambia, the Zambezi River flows through eastern Angola, following the border between Zambia and Zimbabwe before flowing across Mozambique, where it enters the Mozambique Channel through an extensive delta system (Euroconsult Mott MacDonald, 2008). Annual precipitation across the Zambezi Catchment varies spatially with ~150 cm/y in the northern catchments, ~85 cm/y in the southern part, and 60–70 cm/y in the central part (Ronco et al., 2006). This spatial variability is controlled by the seasonal interplay of the Intertropical Convergence Zone (ITCZ) and the Congo Air Boundary (CAB), which collectively separates the Indian and Atlantic Ocean air masses (Figure F1), with the southwest monsoon and the southeast trade winds influencing the upper Zambezi River (i.e., upstream of Victoria Falls) and the northeast monsoon and the southeast trade winds affecting the middle and lower Zambezi River (Moore et al., 2008). Peak precipitation in the Zambezi River basin catchment occurs during the austral summer (December, January, February), when the ITCZ is located at its most southerly position.

The mean outflow of the Zambezi River is 3000 m³/s (Gammelsrød, 1992), and it transports an annual sediment load of ~51 Mm³, making it the largest single source of suspended sediment supply to the Mozambique margin (Walford et al., 2005). The Zambezi delta is located in a moderate indentation of the continental margin. At present, the southward water flow through the Mozambique Channel drives a counter-circulation loop on the shelf, leading to a coastparallel flow that transports sediment toward the northern shelf area in a "mud belt" (Beiersdorf et al., 1980; Schulz et al., 2011; Siddorn et al., 2001) (Figure F2). To the north, this sediment passes over the shelf edge, as well as feeds the submarine Zambezi Canyon (Schulz et al., 2011). The river-borne sediment mixes with currenttransported and biogenic material and is a major component of the extensive current-controlled sedimentary deposits that characterize the Mozambique margin. This system provides the potential to provide comprehensive proxy records that document regional oceanographic changes as well as changes in hydrological conditions of the African precipitation belt in southeastern Africa (e.g., Just et al., 2014; Schefuß et al., 2011; Schulz et al., 2011; Wang et al., 2013; Weldeab et al., 2013, 2014; van der Lubbe et al., 2014, 2015).

¹ Hall, I.R., Hemming, S.R., LeVay, L.J., Barker, S., Berke, M.A., Brentegani, L., Caley, T., Cartagena-Sierra, A., Charles, C.D., Coenen, J.J., Crespin, J.G., Franzese, A.M., Gruetzner, J., Han, X., Hines, S.K.V., Jimenez Espejo, F.J., Just, J., Koutsodendris, A., Kubota, K., Lathika, N., Norris, R.D., Periera dos Santos, T., Robinson, R., Rolinson, J.M., Simon, M.H., Tangunan, D., van der Lubbe, J.J.L., Yamane, M., and Zhang, H., 2017. Site U1477. In Hall, I.R., Hemming, S.R., LeVay, L.J., and the Expedition 361 Scientists, South African Climates (Agulhas LGM Density Profile). Proceedings of the International Ocean Discovery Program, 361: College Station, TX (International Ocean Discovery Program). http://dx.doi.org/10.14379/iodp.proc.361.106.2017

² Expedition 361 Scientists' addresses.

Figure F1. Location map of Site U1477 with main surface currents (arrows) in the southwest Indian Ocean and atmospheric circulation over southern Africa during austral summer (December, January, February) with approximate position of the Intertropical Convergence Zone (ITCZ) and Congo Air Boundary (CAB) (dashed lines; adapted from Reason et al., 2006). AC = Agulhas Current, SEC= South Equatorial Current, SEMC = South East Madagascar Current, NEMC = North East Madagascar Current, EACC = East Africa Coastal Current. Purple shading = Zambezi Catchment, green shading = Limpopo Catchment, TB = Transkei Basin, gray double-headed arrows = main pathways of moisture supply to the African continent from the northwest Atlantic (through Congo) and the northwest and southwest Indian Ocean.



In contrast to the modern sedimentary routing, during the last glacial period when sea level was lower, downslope sediment transport occurred through the Zambezi paleochannel (Chinde-Zambezi paleochannel; Figure F2) located directly off the Zambezi delta. While active, the Zambezi paleochannel prograded toward the present-day shelf edge and incised the wide, subaerially exposed shelf, delivering sediment directly to the upper slope of the western Mozambique Channel (Beiersdorf et al., 1980; Schulz et al., 2011; van der Lubbe et al., 2014). The channelized sediment transport was drastically reduced as the Zambezi paleochannel was rapidly filled during the sea level rise of the last deglaciation, and sediment transport was diverted toward the northern shelf as the coastal current was established on the flooded shelf (van der Lubbe et al., 2014).

Site U1477 is situated on a contourite drift body deposited under the influence of the eddy-dominated water flow through the Mozambique Channel (Figures F3, F4, F5, F6, F7). The drift body displays packages of parallel and laterally continuous subseafloor reflectors (Figures F3, F5, F7). The site is located immediately southwest of the 6.51 m long marine sediment Core GeoB9307-3 (18°33.99′S, 37°22.89′E; 542 mbsl) (Schefuß et al., 2011). Core GeoB9307-3 is in an area of elevated deglacial and Holocene sedimentation. Accelerator mass spectrometry ¹⁴C dates indicate the age at the base of Core GeoB9307-3 is ~17 ky BP (before present). X-ray fluorescence downcore scans show large increases in elemen-

Figure F2. Geomorphologic and oceanographic features near Site U1477. The southward water flow through the Mozambique Channel drives a counter-circulation loop on the shelf (indicated with dashed black lines with arrows), leading to a coast-parallel flow that transports sediment toward the northern shelf area in a "mud belt" (Beiersdorf et al., 1980; Schulz et al., 2011; Siddorn et al., 2001). Approximate location of inner mud belt is shown in brown. Brown arrows = transport directions of major sediment redistribution. Dashed red arrow = bottom water currents, solid arrows = main surface currents. NADW = North Atlantic Deep Water, AAIW = Antarctic Intermediate Water. CZC (purple waved lines) = Chinde-Zambezi paleochannel of the Zambezi River adapted from Schulz et al. (2011). Purple lines indicate the locations of Geophysics Lines M753-GeoB08-192 and 200.

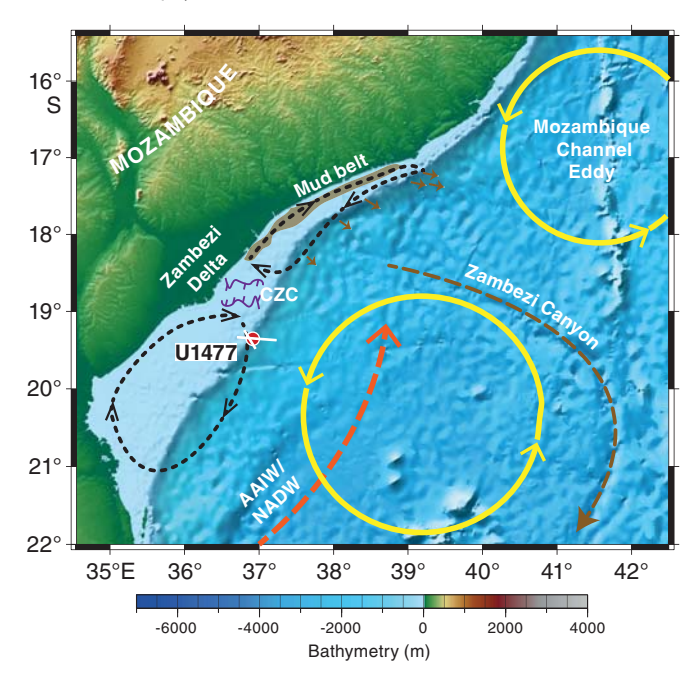
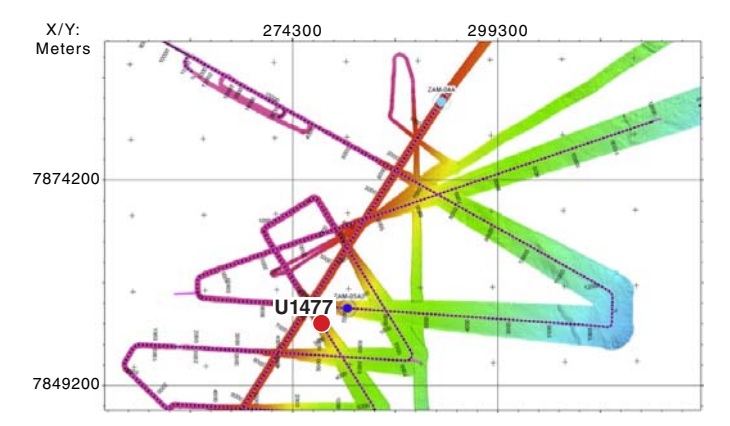


Figure F3. Multibeam bathymetry around Site U1477 showing a generally smooth surface. The overall morphology is shaped by currents, leading to rapid depression fill and winnowing in exposed locations. Drift deposits are attached to the upper slope in 100–1000 m water depth, whereas in deeper water mass wasting areas, channel-levee complexes and erosion dominate.



tal ratios that indicate sedimentary terrestrial contibutions. Large increases in concentrations of terrestrial plant—derived long-chain *n*-alkanes during Heinrich Stadial 1 and the Younger Dryas indicate enhanced terrestrial discharge by the Zambezi River and thus higher rainfall amounts in the catchment (Schefuß et al., 2011). The

Figure F4. Seismic Line M753-GeoB08-200 at Site U1477. Six seismic units (A–F) are marked by distinct but mostly concordant reflectors. Units A–D reveal a sigmoidal shape indicative of contourite deposits. In greater water depths (>1 s two-way traveltime [TWT]), reflectors are wavy or disturbed, which is typical for mass wasting units. In Units E and F, disturbances are more pronounced. Between 0.25 and 1.00 s TWT, surface sediment appears well layered and undisturbed; otherwise, disturbances vary locally. SP = shot point.

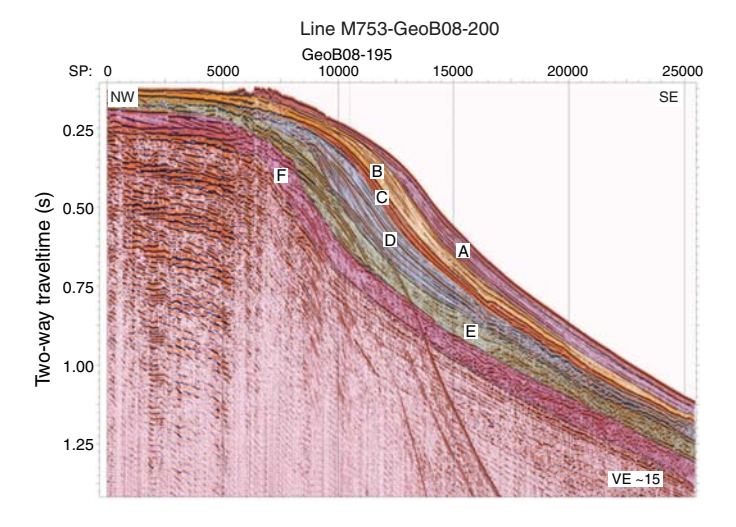
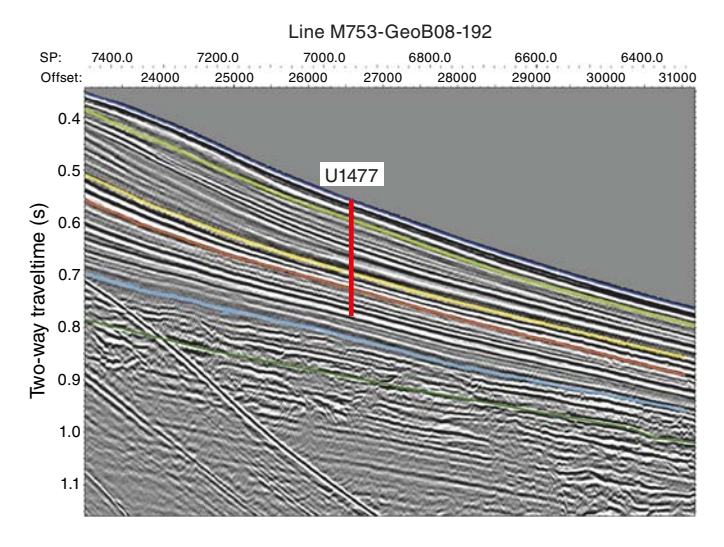


Figure F5. Seismic Line M753-GeoB08-192 at Site U1477.



existing proxy records from Core GeoB9307-3 suggest the great potential of Site U1477 for paleoceanographic research at centennial timescales.

The Site U1477 precruise objectives were to

- Recover a complete and high-resolution sedimentary succession that spans the last 2 my, including the mid-Pleistocene transition (MPT), from the Mozambique margin close to the Zambezi River delta:
- Generate a high-resolution Pleistocene profile of southern African continental climate changes on orbital and suborbital timescales;
- Establish linking between southern African terrestrial climates and southwest Indian Ocean heat budgets, notably warm-water

Figure F6. Detail of seismic Line M753-GeoB08-192 at Site U1477.

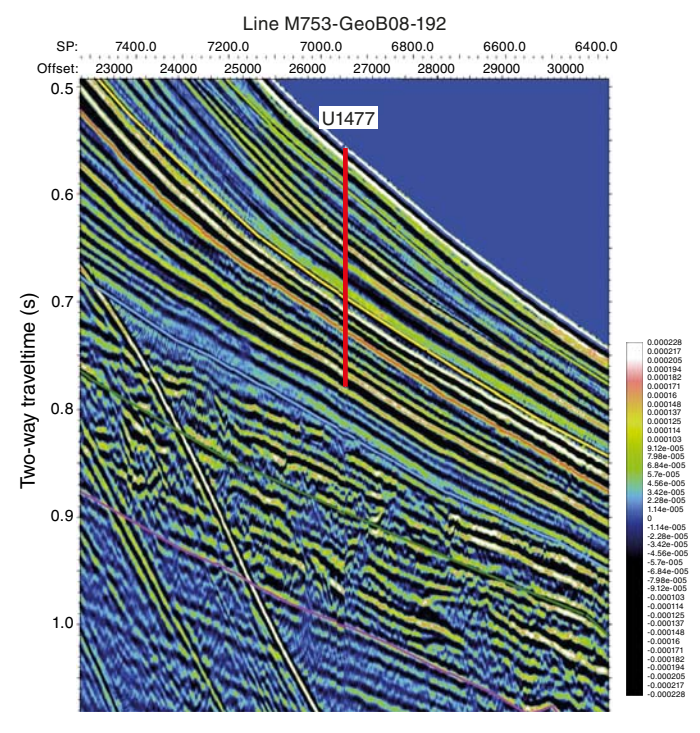
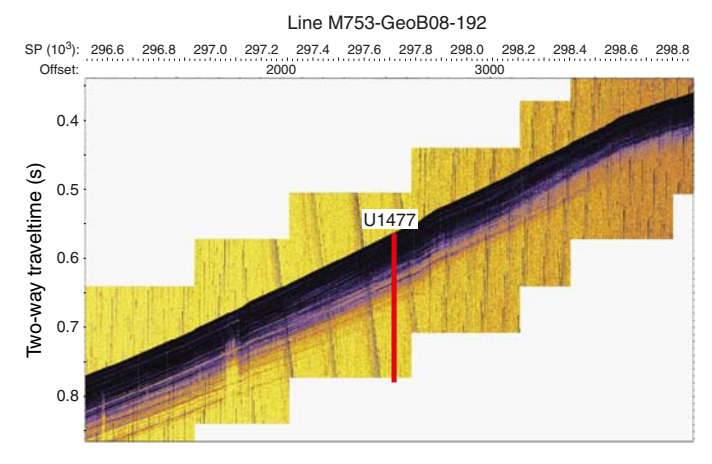


Figure F7. Parasound data along seismic Line M753-GeoB08-192 across Site U1477.



transports along the southeast African margin and associated ocean-atmosphere heat and moisture transfer;

- Examine the relationship between such climate variability and early human evolution; and
- Reconstruct upstream control on Agulhas leakage through headwater variability (Mozambique Current) during periods of orbitally modulated and suborbitally accelerated climate changes.

As detailed in subsequent sections, the actual sequence recovered featured greatly elevated accumulation rates and did not penetrate through the Late Pleistocene. Thus, the specific questions that will be addressed include the following: How did the rainfall patterns over southeast Africa evolve during the course of the last ice age cycle, notably in conjunction with monsoon dynamics, and mi-

gration of the ITCZ (Johnson et al., 2002; Schefuß et al., 2011; Trauth et al., 2009)? Did variable Agulhas Current warm-water transports contribute to and modulate the impacts of shifting air boundaries and rainfall patterns over southeast Africa and possibly offset these patterns from those over southwest Africa and the Namib (Dupont et al., 2005; 2011; Maslin et al. 2012)?

Site U1477 was occupied on 13 March 2016. Three holes were drilled and cored using the advanced piston corer (APC), half-length APC (HLAPC), and extended core barrel (XCB), achieving a depth of 181.2 m drilling depth below seafloor (DSF) in Hole U1477A. The total cored interval at Site U1477 was 474 m, and total recovery was 490.03 m (103%).

Operations

Transit to Site U1477

After a 350 nmi transit from Site U1476, the vessel arrived at proposed Site ZAM-05A (Site U1477) at 0942 h on 13 March 2016, and the thrusters were lowered at 1015 h.

Site U1477

Site U1477 consisted of 3 holes, ranging in depth from 119.4 to 181.2 m DSF (Table **T1**). Overall, 69 cores were recorded for the site. A total of 308.07 m of core over a 296.2 m interval was recovered using the APC system (104% core recovery). The HLAPC re-

Table T1. Site U1477 core summary. DRF = drilling depth below rig floor, DSF = drilling depth below seafloor, CSF = core depth below seafloor. H = APC core, F = HLAPC core, X = XCB core, numeric core type = drilled interval. (Continued on next page.) **Download table in .csv format.**

Hole U1477A

Latitude: 19°21.2930′S Longitude: 36°54.8962′E Time on hole (h): 20.0

Seafloor (drill pipe measurement below rig floor, m DRF): 440.4 Distance between rig floor and sea level (m): 11.2

Water depth (drill pipe measurement from sea level, mbsl): 429.2 Total penetration (drilling depth below seafloor, m DSF): 181.2

Total length of cored section (m): 181.2 Total core recovered (m): 182.53 Core recovery (%): 101 Total number of cores: 27

Hole U1477C

Latitude: 19°21.2928′S Longitude: 36°54.9066′E Time on hole (h): 11.5

Seafloor (drill pipe measurement below rig floor, m DRF): 440.4

Distance between rig floor and sea level (m): 11.2

Water depth (drill pipe measurement from sea level, mbsl): 429.2

Total penetration (drilling depth below seafloor, m DSF): 119.4

Total length of cored section (m): 118.4 Total core recovered (m): 121.75

Core recovery (%): 103 Total number of cores: 16

Hole U1477B

Latitude: 19°21.2822′S Longitude: 36°54.8958′E Time on hole (h): 13.0

Seafloor (drill pipe measurement below rig floor, m DRF): 440.8

Distance between rig floor and sea level (m): 11.2

Water depth (drill pipe measurement from sea level, mbsl): 429.6 Total penetration (drilling depth below seafloor, m DSF): 174.4

Total length of cored section (m): 174.4 Total core recovered (m): 185.73

Core recovery (%): 106 Total number of cores: 26

			Depth	DSF (m)		Depth	CSF (m)	Length of				
Core	Date (2016)	Time UTC (h)	Top of cored interval	Bottom of cored interval	f Interval advanced (m)	Top of cored interval	Bottom of cored interval	core recovered (m)	Recovery (%)	Sections (N)		
361-U147	77A-											
1H	13 Mar	1345	0.0	7.5	7.5	0.0	7.56	7.56	101	6		
2H	13 Mar	1415	7.5	17.0	9.5	7.5	17.30	9.80	103	8		
3H	13 Mar	1440	17.0	26.5	9.5	17.0	26.88	9.88	104	8		
4H	13 Mar	1505	26.5	36.0	9.5	26.5	36.68	10.18	107	8		
5H	13 Mar	1525	36.0	45.5	9.5	36.0	46.30	10.30	108	8		
6H	13 Mar	1550	45.5	55.0	9.5	45.5	55.68	10.18	107	8		
7H	13 Mar	1620	55.0	64.5	9.5	55.0	65.28	10.28	108	8		
8H	13 Mar	1645	64.5	74.0	9.5	64.5	74.47	9.97	105	9		
9H	13 Mar	1715	74.0	83.5	9.5	74.0	82.98	8.98	95	7		
10H	13 Mar	1745	83.5	93.0	9.5	83.5	93.07	9.57	101	8		
11H	13 Mar	1840	93.0	102.5	9.5	93.0	101.89	8.89	94	8		
12F	13 Mar	1935	102.5	107.2	4.7	102.5	107.45	4.95	105	5		
13F	13 Mar	2000	107.2	111.9	4.7	107.2	111.85	4.65	99	5		
14F	13 Mar	2030	111.9	116.6	4.7	111.9	116.95	5.05	107	5		
15F	13 Mar	2050	116.6	121.3	4.7	116.6	121.52	4.92	105	5		
16F	13 Mar	2115	121.3	126.0	4.7	121.3	126.08	4.78	102	5		
17F	13 Mar	2145	126.0	130.7	4.7	126.0	130.97	4.97	106	5		
18F	13 Mar	2205	130.7	135.4	4.7	130.7	135.62	4.92	105	5		
19F	13 Mar	2235	135.4	140.1	4.7	135.4	139.89	4.49	96	4		
20F	13 Mar	2300	140.1	144.8	4.7	140.1	145.07	4.97	106	5		
21F	13 Mar	2330	144.8	149.5	4.7	144.8	148.69	3.89	83	4		
22F	13 Mar	2350	149.5	154.2	4.7	149.5	153.80	4.30	91	4		

Table T1 (continued).

-			Depth DSF (m)		Depth CSF (m)			Length of		
Core	Date (2016)	Time UTC (h)	Top of cored interval	Bottom of cored interval	Interval advanced (m)	Top of cored interval	Bottom of cored interval	core recovered (m)	Recovery (%)	Sections (<i>N</i>)
23F	14 Mar	0020	154.2	158.9	4.7	154.2	159.29	5.09	108	5
24F	14 Mar	0045	158.9	163.6	4.7	158.9	161.39	2.49	53	3
25F	14 Mar	0105	163.6	168.3	4.7	163.6	168.60	5.00	106	6
26F	14 Mar	0135	168.3	173.0	4.7	168.3	172.81	4.51	96	5
27X	14 Mar	0240	173.0	181.2	8.2	173.0	180.96	7.96	97	7
361-U147	77B-									
1H	14 Mar	0520	0.0	4.1	4.1	0.0	4.13	4.13	101	4
2H	14 Mar	0540	4.1	13.6	9.5	4.1	13.82	9.72	102	8
3H	14 Mar	0605	13.6	23.1	9.5	13.6	23.54	9.94	105	8
4H	14 Mar	0625	23.1	32.6	9.5	23.1	33.31	10.21	107	8
5H	14 Mar	0650	32.6	42.1	9.5	32.6	42.81	10.21	107	8
6H	14 Mar	0715	42.1	51.6	9.5	42.1	52.15	10.05	106	8
7H	14 Mar	0740	51.6	61.1	9.5	51.6	61.97	10.37	109	8
8H	14 Mar	0805	61.1	70.6	9.5	61.1	71.95	10.89	115	9
9H	14 Mar	0830	70.6	80.1	9.5	70.6	81.33	10.73	113	9
10H	14 Mar	0855	80.1	89.6	9.5	80.1	90.92	10.82	114	10
11H	14 Mar	0930	89.6	99.1	9.5	89.6	98.65	9.05	95	7
12H	14 Mar	1000	99.1	108.6	9.5	99.1	108.24	9.14	96	8
13F	14 Mar	1035	108.6	113.3	4.7	108.6	113.91	5.31	113	6
14F	14 Mar	1055	113.3	118.0	4.7	113.3	118.61	5.31	113	6
15F	14 Mar	1120	118.0	122.7	4.7	118.0	123.36	5.36	114	6
16F	14 Mar	1140	122.7	127.4	4.7	122.7	127.77	5.07	108	5
17F	14 Mar	1200	127.4	132.1	4.7	127.4	132.71	5.31	113	5
18F	14 Mar	1225	132.1	136.8	4.7	132.1	136.97	4.87	104	5
19F	14 Mar	1245	136.8	141.5	4.7	136.8	142.04	5.24	111	5
20F	14 Mar	1310	141.5	146.2	4.7	141.5	146.50	5.00	106	5
21F	14 Mar	1335	146.2	150.9	4.7	146.2	151.45	5.25	112	6
22F	14 Mar	1355	150.9	155.6	4.7	150.9	156.06	5.16	110	6
23F	14 Mar	1415	155.6	160.3	4.7	155.6	160.10	4.50	96	5
24F	14 Mar	1440	160.3	165.0	4.7	160.3	164.95	4.65	99	5
25F	14 Mar	1500	165.0	169.7	4.7	165.0	169.28	4.28	91	4
26F	14 Mar	1525	169.7	174.4	4.7	169.7	174.86	5.16	110	5
361-U147	77C-									
11	14 Mar	1750		*****	Orilled interva	al 0–1.0 m D	SF****			
2H	14 Mar	1805	1.0	10.5	9.5	1.0	10.03	9.03	95	7
3H	14 Mar	1830	10.5	20.0	9.5	10.5	20.31	9.81	103	8
4H	14 Mar	1855	20.0	29.5	9.5	20.0	29.98	9.98	105	8
5H	14 Mar	1920	29.5	39.0	9.5	29.5	39.56	10.06	106	8
6H	14 Mar	1950	39.0	48.5	9.5	39.0	48.82	9.82	103	8
7H	14 Mar	2010	48.5	58.0	9.5	48.5	58.40	9.90	104	8
8H	14 Mar	2045	58.0	67.5	9.5	58.0	68.32	10.32	109	9
9H	14 Mar	2115	67.5	77.0	9.5	67.5	77.36	9.86	104	8
10H	14 Mar	2145	77.0	86.5	9.5	77.0	85.44	8.44	89	6
11F	14 Mar	2210	86.5	91.2	4.7	86.5	91.44	4.94	105	5
12F	14 Mar	2235	91.2	95.9	4.7	91.2	96.10	4.90	104	5
13F	14 Mar	2300	95.9	100.6	4.7	95.9	100.96	5.06	108	5
14F	14 Mar	2320	100.6	105.3	4.7	100.6	105.78	5.18	110	5
15F	14 Mar	2345	105.3	110.0	4.7	105.3	110.27	4.97	106	5
16F	15 Mar	0005	110.0	114.7	4.7	110.0	114.85	4.85	103	5
17F	15 Mar	0035	114.7	119.4	4.7	114.7	119.35	4.65	99	5

covered 174.00 m of sediment over a 169.2 m interval (103% core recovery). The XCB was deployed for one core resulting in 7.96 m of sediment (97% core recovery). One interval was advanced without coring over 1.0 m. Overall, at total of 490.03 m of core was retrieved from a 474.0 m cored interval at Site U1477 (103% core recovery). The total time spent at Site U1477 was 1.9 days.

Hole U1477A

The APC/XCB bottom-hole assembly (BHA) and drill string were deployed to $412.2\ mbsl$. The first two coring attempts resulted

in water cores and, after lowering the bit a total of 15 m, Hole U1477A was spudded at 1535 h on 13 March 2016. Core 361-U1477A-1H recovered 7.52 m of sediment, and the water depth was calculated at 429.2 mbsl. The hole was cored to 102.5 m DSF (Cores 1H through 11H) using the APC system. After partial strokes with the APC on Cores 10H and 11H, the HLAPC was deployed, and piston coring continued to 173.0 m DSF (Cores 12F through 26F). The XCB was deployed for Core 27X (173.0–181.2 m DSF). Coring was terminated in Hole U1477A at a total depth of 181.2 m DSF. The drill string was removed from the hole, with the bit clearing the sea-

floor at 0615 h on 14 March, ending Hole U1477A. The total core recovery for Hole U1477A was 182.53 m over a 181.2 m cored interval (101%).

Hole U1477B

The vessel was offset 20 m north of Hole U1477A, and Hole U1477B was spudded at 0705 h on 14 March. The APC system was deployed for Cores 361-U1477B-1H through 12H (0–108.6 m DSF). After two partial strokes with the APC, the HLAPC was used for Cores 13F through 26F (108.6–174.4 m DSF). A total of 185.73 m of core was recovered over a 174.4 m cored interval in Hole U1477B (106%). The drill string was pulled from the hole, and the bit cleared the seafloor at 1910 h on 14 March, ending Hole U1477B.

Hole U1477C

The vessel was offset 20 m east of Hole U1477A, and Hole U1477C was spudded at 1950 h on 14 March with a 1.0 m drilled interval. The APC system was used for Cores 361-U1477C-2H through 10H. After partial stokes on Cores 9H and 10H, the HLAPC was deployed for Cores 11F through 17F. Coring was terminated at a total depth of 119.4 m DSF. One partial stroke was recorded while using the HLAPC (Core 12F). A total of 121.77 m of core was recovered from a 118.4 m cored interval (103%). The drill string was pulled from the hole, with the bit clearing the seafloor at 0415 h and the rotary table at 0555 h on 15 March. The rig floor was secured for transit at 0630 h, and the vessel was under way to Site U1478 at 0642 h, ending Site U1477.

Sedimentology

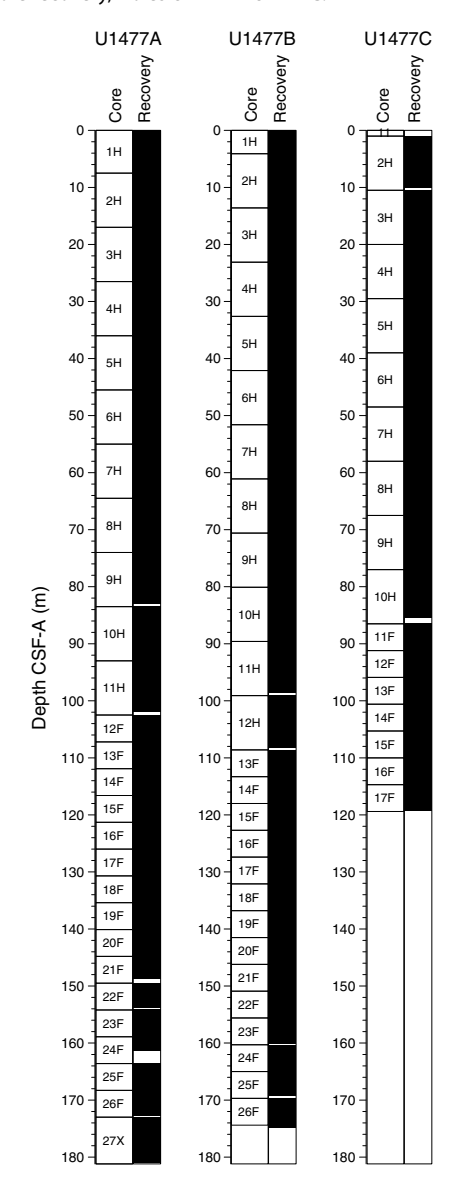
Drilling at Site U1477 recovered a total of ~490 m of sediment from three holes (Figures F8, F9; also see Operations). Hole U1477A was cored to 180.96 m coring depth below seafloor (CSF-A), Hole U1477B to 174.86 m CSF-A, and Hole U1477C to 119.35 m CSF-A. The APC system was applied in the uppermost ~100 m CSF-A of Hole U1477A, ~110 m CSF-A of Hole U1477B, and ~90 m CSF-A of Hole U1477C. The HLAPC was used in the lower parts of all holes, and the XCB was used for the deepest core in Hole U1477A (Core 361-U1477A-27X). One interval >1 m was advanced without coring in Hole U1477C (0-1.0 m CSF-A). A visual description of all cores was performed and recorded using the shipboard lithostratigraphic DESClogik program, which involves visual assessment of average grain size, sediment color, sedimentary structures, and bioturbation intensity. Disturbances induced by drilling and gas expansion were also described. Lithologic characteristics were further determined using smear slide analyses, and a total of 304 shipboard samples were collected from the working halves of the cores from Holes U1477A and U1477C for paleontological, physical property, paleomagnetic, and geochemical analyses (Table T2).

Lithostratigraphic unit description

Unit I

Intervals: 361-U1477A-1H-1, 0 cm, through 1H-2, 144 cm; 361-U1477B-1H-1, 0 cm, through 1H-3, 87 cm; 361-U1477C-2H-1, 0 cm, through 2H-2, 150 cm Depths: Hole U1477A = 0–3.00 m CSF-A; Hole U1477B = 0–3.87 m CSF-A; Hole U1477C = 1.00–4.00 m CSF-A Age: Holocene

Figure F8. Core recovery, Holes U1477A-U1477C.



Unit I is composed of very dark gray (5Y 3/1) and dark gray (7.5YR 4/1) to dark greenish gray (GLEY 1 4/10Y; 10YR 3/1) sandy clay with foraminifers and nannofossils (Figure **F10**).

Unit II

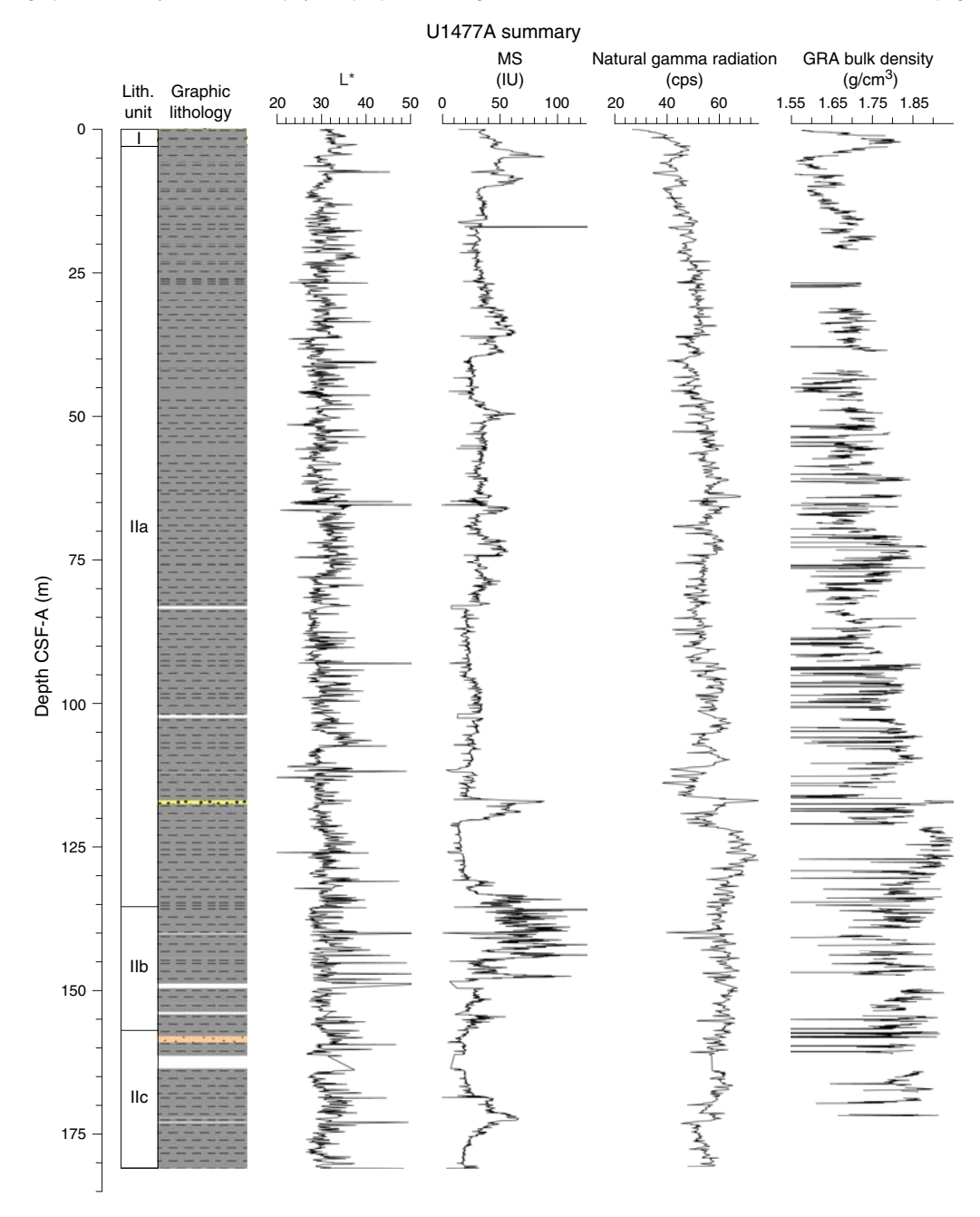
Subunit Ila

Intervals: 361-U1477A-1H-3, 0 cm, through 18F-CC, 17 cm; 361-U1477B-1H-CC, 0 cm, through 17F-CC, 32 cm; 361-U1477C-2H-3, 0 cm, through 17F-CC, 32 cm Depths: Hole U1477A = 3.00–135.62 m CSF-A; Hole U1477B = 3.87–132.71 cm CSF-A; Hole U1477C = 4.00–119.35 m CSF-A

Age: Late Pleistocene to Holocene

Subunit IIa is composed of very dark gray (5Y 3/1; 10YR 3/1; GLEY I 3/N), dark greenish gray (GLEY 1 4/5GY), and occasionally

Figure F9. Lithostratigraphic summary with selected physical properties and geochemical data. Hole U1477A. (Continued on next two pages.)



olive-gray (5Y 5/3) silty clay, with intermittent occurrences of sand or light brown silt/clay layers (Figure **F10**).

Subunit IIb

Intervals: 361-U1477A-19F-1, 0 cm, through 23F-2, 137 cm; 361-U1477B-18F-1, 0 cm, through 22F-CC, 10 cm. Depths: Hole U1477A = 135.4-156.94 m CSF-A; Hole U1477B = 132.1-156.06 m CSF-A. Age: Late Pleistocene

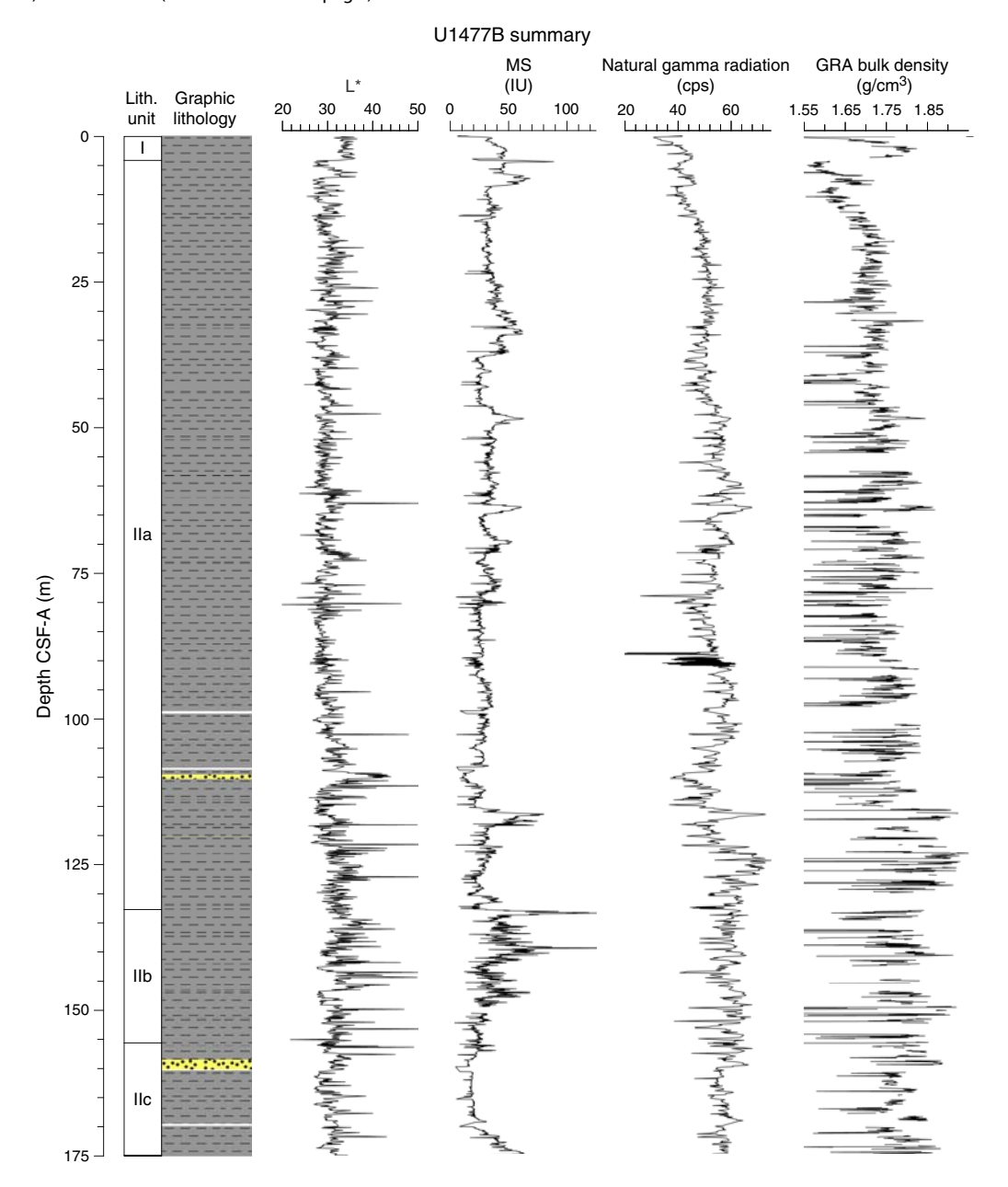
Subunit IIb is characterized by very dark gray (5Y 3/1; 10YR 3/1; GLEY I 3/N) silty clay with frequent occurrences of sand or light brown silt/clay layers (Figure **F10**).

Subunit IIc

Intervals: 361-U1477A-23F-3, 0 cm, through 27X-CC, 31 cm; 361-U1477B-23F-1, 0 cm through 26F-CC, 12 cm. Depths: Hole U1477A = 156.94–180.96 m CSF-A; Hole U1475B = 155.60–174.86 m CSF-A.

Age: Late Pleistocene

Figure F9 (continued). Hole U1477B. (Continued on next page.).



Subunit IIc is composed of very dark gray (5Y 3/1; 10YR 3/1; GLEY I 3/N) silty clay with intermittent occurrences of sand or light brown silt/clay layers (Figure **F10**). Lithologic features resemble those of Subunit IIa.

Drilling disturbance

Cores from Site U1477 show severe drilling disturbances (fractures and fragmented intervals and voids) related to gas expansion. The uppermost centimeters of the first sections of some cores are soupy (Sections 361-U1477A-2H-1, 4H-1, 9H-1, 11H-1, and 16F-1; 361-U1477B-5H-1; and 361-U1477C-3H-1 and 6H-1); fractures are typically observed in the middle to bottom sections of most cores (Figure F11). "Biscuits" from drilling disturbance were observed in Core 361-U1477A-27X. Differences in lithologies in the uppermost <10 cm of the first core of Holes U1477B and U1477C in compari-

son to that in Hole U1477A may be attributed to drilling disturbances (fall-in). Specifically, dark gray silty clays, which are typical for Unit II, are present at the top of Holes U1477B and U1477C but not Hole U1477A. These clays in Hole U1477B show nannofossil assemblages that are similar to those described in core catchers from deeper intervals of Hole U1477A (see **Micropaleontology**), supporting the inference of potential contamination of the uppermost few centimeters of Holes U1477B and U1477C.

Lithologies and composition

Smear slide observations show that siliciclastic materials (87% \pm 8% on average) are the principal component of the sediment at Site U1477 (Table **T3**; Figure **F12**). In Unit I, the sediment grain sizes consist of 28% (±15%) sand on average, 26% (±11%) silt, and 46% (±8%) clay. The sediment grain sizes consist of 11% (±5%) sand, 37%

Figure F9 (continued). Hole U1477C.

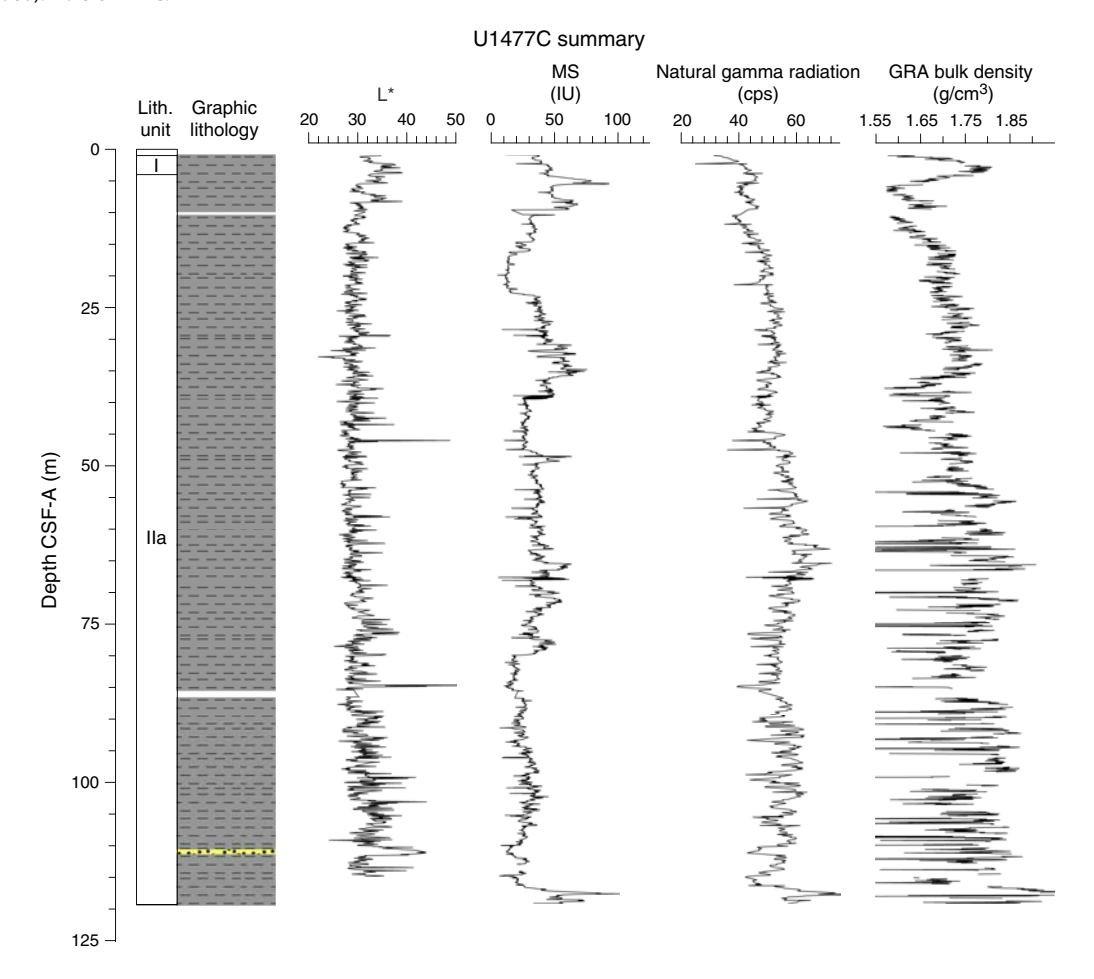


Table T2. Overview of shipboard sampling with number of samples taken, Holes U1477A–U1477C. NANNO = nannofossils, PMAG = paleomagnetism, MAD = moisture and density, FORAM = foraminifers, CARB = carbonate, DIAT = diatoms. A = archive, W = working. TPCK = toothpick, CYL = cylinder, OTHR = other. **Download table in .csv format.**

Sample type	Section half	Sample tool	Hole U1477A	Hole U1477B	Hole U1477C	Total
Smear slide	Α	TPCK	33	28	19	80
NANNO	W	TPCK	30	0	0	30
PMAG	W	CUBE (7 cm ³)	16	0	14	30
MAD	W	CYL (10 cm ³)	61	0	0	61
FORAM	W	CYL (10 cm ³)	26	0	0	26
CARB	W	CYL (5 cm ³)	47	0	0	47
DIAT	W	OTHR	30	0	0	30
		Total:	243	28	33	304

($\pm 5\%$) silt, and 52% ($\pm 5\%$) clay in Subunit IIa and 8% ($\pm 2\%$) sand, 41% ($\pm 4\%$) silt, and 51% ($\pm 3\%$) clay in Subunit IIc. The quartz-rich sand layers in Subunit IIb consist of 75% sand, 13% silt, and 12% clay, whereas the aragonite-rich silt/clay layers in the same subunit consist of 6% ($\pm 1\%$) sand, 15% ($\pm 1\%$) silt, and 80% ($\pm 2\%$) clay.

The composition of the siliciclastic component is dominated by clay minerals (34% \pm 15%) and quartz (32% \pm 11% on average) in both units. Pyrite (7% \pm 5% on average) and biotite (4% \pm 2%) are also present throughout the cores. Trace amounts of zircon, hornblende, plagioclase, and dolomite were also regularly registered. These minerals are more abundant (1–6%) in medium sand–sized layers occasionally recorded in both units. The light brown silt/clay

layers consist of 70% (±4%) carbonate fragments, in which needle-shaped crystals may likely be aragonite.

Biogenic materials represent only $8\% \pm 6\%$ on average of the sediment. In Unit I, the biogenic fraction is larger ($21\% \pm 11\%$ on average) and is dominated by nannofossils ($10\% \pm 6\%$) and foraminifers ($8\% \pm 5\%$). In Unit II, the biogenic fraction is dominated by foraminifers ($3\% \pm 2\%$) and nannofossils ($2\% \pm 2\%$). The average abundance of total biogenic carbonate in the sediment in Hole U1477A was estimated at $4\% \pm 5\%$ based on smear slides descriptions (Table T3). This result is in general agreement with geochemical analyses (see **Geochemistry**), which measured the average carbonate content at ~ 5 wt% (range = 1-22 wt%) (Figure F13).

Figure F10. A–L. Representative lithologies per interval. Section-half (left) surfaces and smear slide photomicrographs taken under plane-polarized (middle) and cross-polarized (right) light, Site U1477. Scale bars = $100 \, \mu m$.

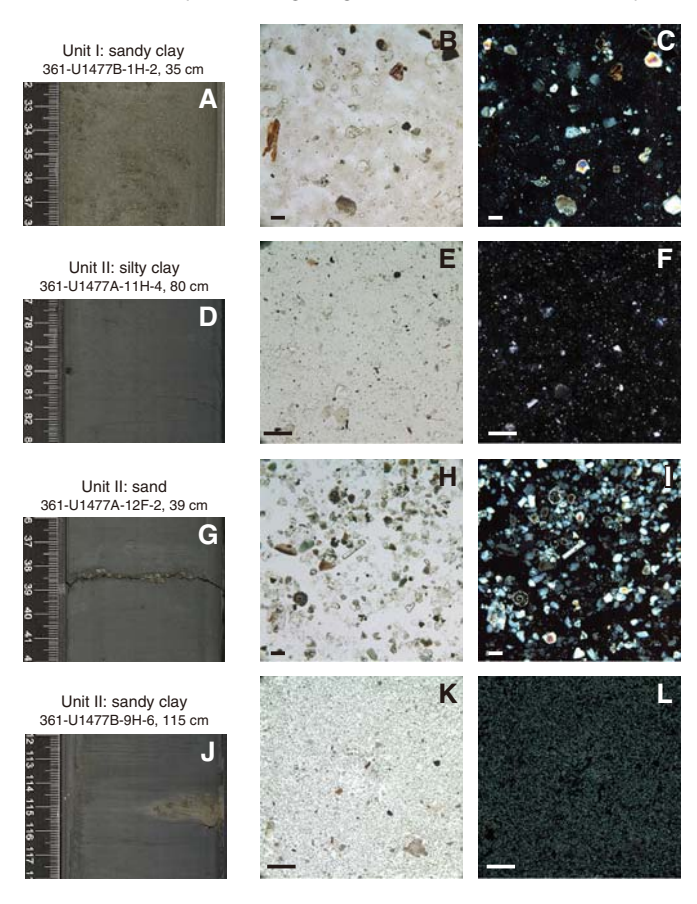


Figure F11. A-G. Sediment deformations and disturbances, Site U1477.

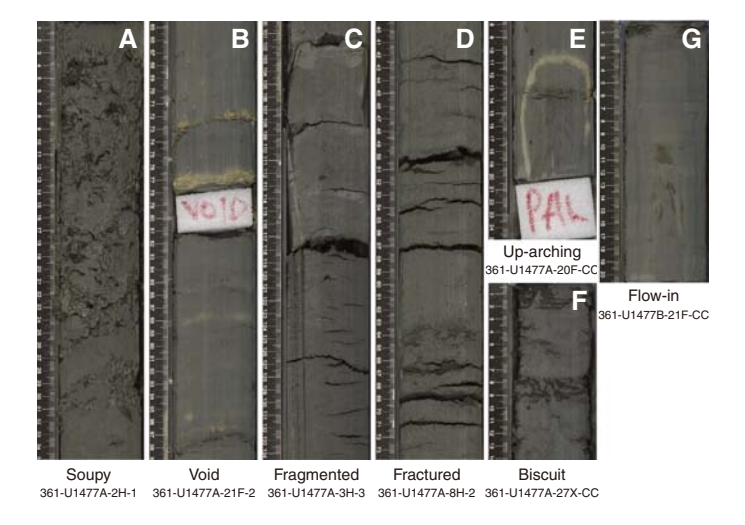


Table T3. Smear slide textures, compositions, and lithologic names, Holes U1477A–U1477C. **Download table in .csv format.**

Structures

No primary sedimentary structures were observed. Visible secondary sedimentary structures, such as bioturbation, are rare. We note, however, that the very dark color of the sediment at Site

Figure F12. Relative percentages of major compositions of sediment determined by smear slide observation, Holes U1477A–U1477C.

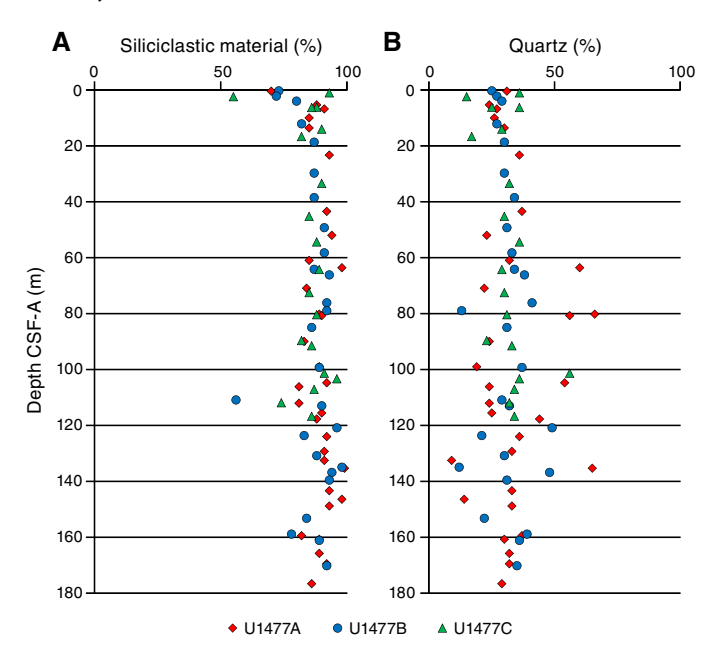
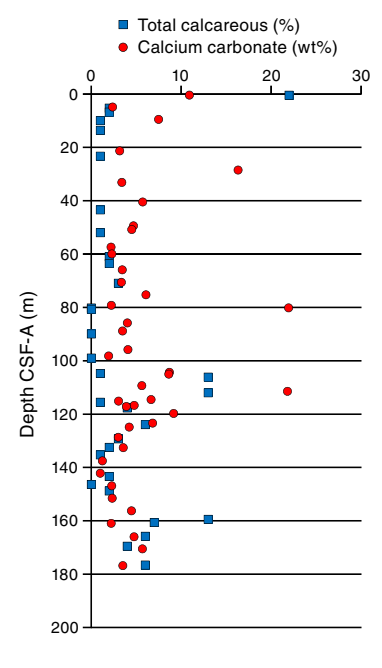


Figure F13. Comparison of $CaCO_3$ content determined using measurements on discrete samples and biogenic carbonate proportions estimated in smear slides, Hole U1477A.



 $\rm U1477~may~obscure~sedimentary~structures~(e.g.,~bioturbation~and~diagenetic~alterations).$

Color

The color of the clayey sand in Unit I ranges between very dark gray (5Y 3/1; 10YR 3/1; GLEY I 3/N) and dark greenish gray (GLEY 1 4/10Y). The color of the silty clay in Subunit IIa ranges between dark gray (7.5YR 4/1; 10YR 4/1; GLEY 1 4/N) and dark greenish gray (GLEY 1 3/5GY) to very dark gray (5Y 3/1; 10YR 3/1). Finally, the silty clay in Subunits IIb and IIc is very dark gray (GLEY 1 3/N).

Discussion

Site U1477 is located in the western Mozambique Channel on the upper continental slope, off the Zambezi River, at a water depth of \sim 429 mbsl. The contourite drift body on which Site U1477 is located was deposited under influence of the eddy-dominated water flow through the Mozambique Channel (Lutjeharms, 2006). Site U1477 receives fluvial material from the Zambezi River, which has a mean outflow of \sim 3000 m³/s (Gammelsrød, 1992). The Zambezi Catchment area is in the southernmost reaches of the African monsoonal precipitation belt and drains multiple subbasins with differing basement lithologies, soils, and vegetation assemblages (e.g., Just et al., 2014; van der Lubbe et al., 2014).

The high proportion of siliciclastic material and the relatively increased amounts of organic matter (see Geochemistry) as well as high sedimentation rates of ~1 m/ky (see Age model) suggest enhanced deposition of Zambezi sediment at Site U1477. A change from sandy clay (Unit I) to silty clay (Unit II) sediment in all holes likely marks the Late Pleistocene/Holocene transition (see Age model) as inferred from correlation to published records from the area (van der Lubbe et al., 2014). This lithologic change can be attributed to the flooding of the Mozambique shelf as a result of sea level rise during the Holocene. A combination of high sea level and changes in oceanic currents during the Holocene can lead to the deposition of finer materials in the Mozambique shelf, whereas during times of low sea level the sediment largely bypasses the shelf and is delivered directly to the margin through the Zambezi paleochannel (van der Lubbe et al., 2014). The frequent occurrence of event layers consisting of quartz (sand/silt fraction) and biogenic carbonate fragments (clay fraction) in Subunit IIb can be attributed to river floods and/or storms enhancing current activity on the Mozambique shelf. These processes could trigger winnowing and downslope transport of coarse-grained sediment.

Physical properties

Physical property measurements were completed on wholeround sections and section halves from cores collected from Holes U1477A-U1477C. Gamma ray attenuation (GRA) density, magnetic susceptibility (MS), P-wave velocity (V_P) , and natural gamma radiation (NGR) measurements were made on all whole-round sections using the Special Task Multisensor Logger (STMSL), the Whole-Round Multisensor Logger (WRMSL), and the Natural Gamma Radiation Logger (NGRL). In all cases, STMSL resolution was set to 5 cm, WRMSL resolution was set to 2.5 cm, and NGRL resolution was set to 10 cm. All sections were first logged using the STMSL without waiting for thermal equilibration, generating a set of GRA density and magnetic susceptibility data that was used for stratigraphic correlation. Following thermal equilibration (after temperature reached 19°C), the sections were logged using the WRMSL, generating V_p , GRA, and magnetic susceptibility data, and then logged using the NGRL.

Following core splitting, samples were taken for moisture and density (MAD) measurements from the working-half sections. The MAD (index) properties determined at Site U1477 include bulk density, dry density, grain density, porosity, void ratio, and water content. Three samples per core from the working-half sections of Holes U1477A were taken for MAD measurements. The samples (61 in total) were taken typically from Sections 2, 4, and 6 with few exceptions based on visual inspection. Spectral color reflectance and magnetic susceptibility were measured at a resolution of 8 cm on the archive-half sections using the Section Half Multisensor Log-

ger (SHMSL). Red, green, and blue (RGB) were measured on the Section Half Imaging Logger (SHIL).

Diffuse reflectance spectrometry and digital color image

Spectral reflectance parameter L* ranges from 22 to 46 and shows a complex pattern (Figure **F14**). A poorly defined cyclic pattern is interrupted by abrupt variations. In the upper 64 m CSF-A, these sharp variations are represented by either increases or decreases in L* values and are between 25 and 40, but below this depth they are mainly associated with increases in L* with one exception at \sim 110 m CSF-A. The interval between \sim 64 and \sim 76 m CSF-A has high average L* values (30.6 \pm 2.8).

Spectral reflectance values for a* and b* are in general between 2.6 and -0.5 and between 2.6 and -6.3, respectively. Maxima in a* and b* values were observed in the mudline core, but a major difference between these reflectance parameters was observed in the upper sections, with maximum values for b* broadly corresponding to lithostratigraphic Unit I (see Sedimentology). On the other hand, maximum values for a* were observed between 5 and 9 m CSF-A, directly below Unit I. In general, a* and b* are poorly correlated, whereas b* shows a broad correspondence with L* values. The most systematic feature is a clear anticorrelation between a* and b* in several of the most prominent peaks along the sequence (e.g., 130, 133, and 158 m CSF-A) and an interval of relatively stable values between 120 and 155 m CSF-A. The color reflectance variations are due to compositional changes (e.g., organic matter versus clay mineral concentration/composition). Spectral reflectance data are very similar between holes. Deviations from good correspondence between holes are attributed to drilling disturbances.

SHIL records of RGB data were obtained from the moist surface of the archive halves of split cores. RGB data have average values of

Figure F14. Color reflectance and NGR, Hole U1477A. Reflectance parameters were filtered to remove outliers.

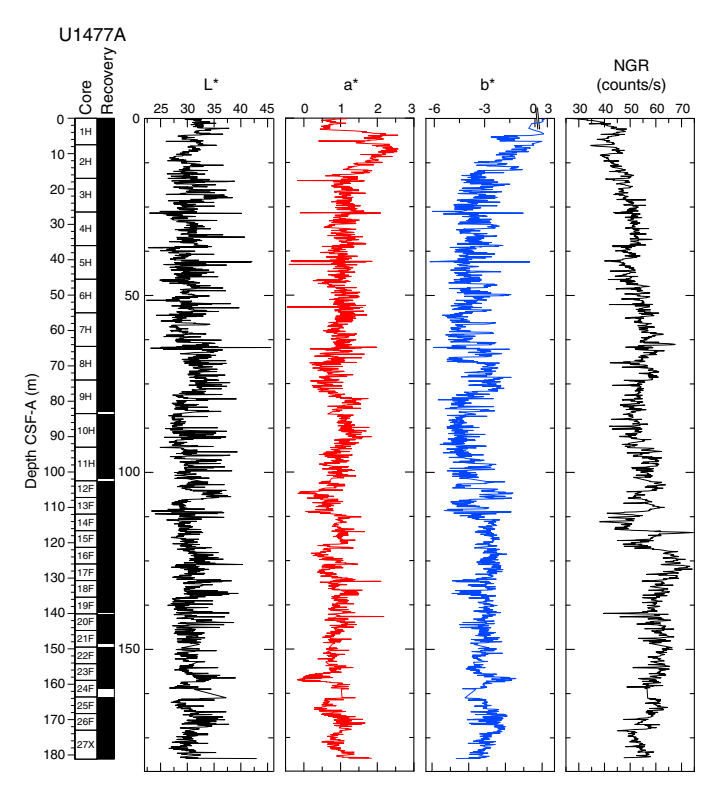
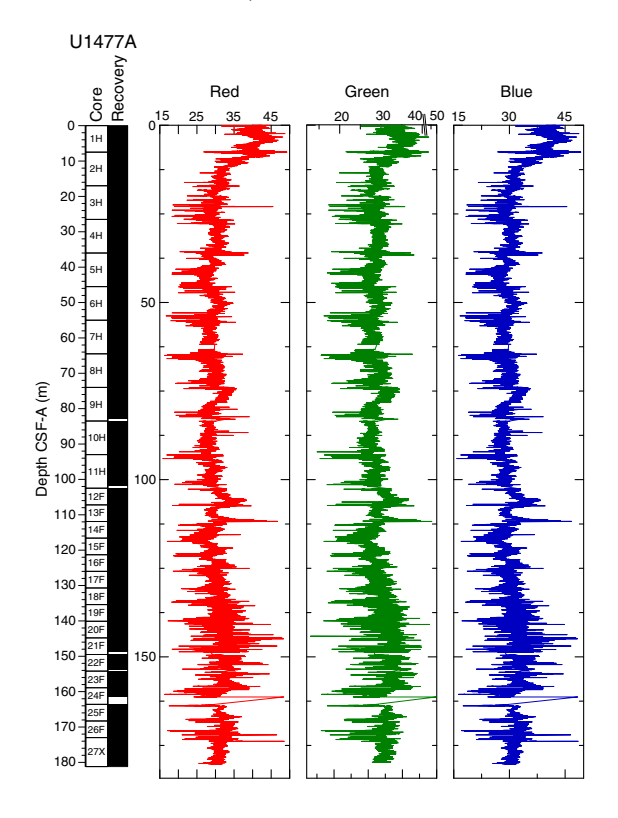


Figure F15. SHIL RGB color data, Hole U1477A.



 $R=31\pm3.4$, $G=31\pm3.1$, and $B=30\pm2.7$ (Figure **F15**). Data also show a complex pattern with high values in the mudline core, stable values interrupted by occasional abrupt variations between 9.5 and $\sim 110\,$ m CSF-A, and high-frequency variations in the lower part. There is some broad correlation with a* in the mudline core, but the data show a variable correlation with other spectral reflectance parameter along the entire sequence.

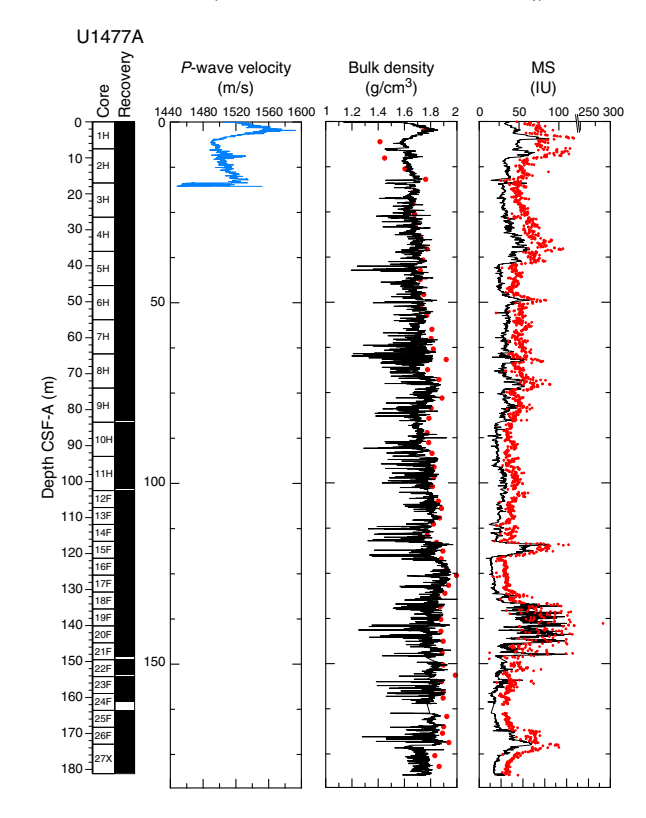
Natural gamma radiation

In Hole U1477A, NGR (Figure **F14**) is 54 ± 7 counts/s on average. In the uppermost 64 m CSF-A, NGR increases from 30 to 67 counts/s. This gradual increase is interrupted by a zone with lower average values (41 counts/s) at 37-46 m CSF-A. Below 64 m CSF-A, NGR shows no clear trends and fluctuates around an average value of 56 ± 5 counts/s. A maximum of 74 counts/s occurs at 117 and ~ 127 m CSF-A, whereas a local minimum was observed at 114 m CSF-A. Spike-like excursions to lower NGR values (e.g., at 140 m CSF-A) may be due to voids caused by gas expansion.

Magnetic susceptibility

Whole-round core (WRMSL) measurements of magnetic susceptibility in Hole U1477A (Figure **F16**) have an average of 35.5 \pm 14.9 instrument units (IU; $\sim 10^{-5}$ SI). The low variability ($\sim 5-10$ IU) background magnetic susceptibility decreases from 37 IU at the seafloor to 19 IU at the bottom of the hole. Superimposed on this trend are numerous 3–7 m intervals with significantly higher magnetic susceptibility values of up to 86 IU. A very prominent feature in the sequence is a zone of high magnetic susceptibility values between 133 and 144 m CSF-A. Within this zone, magnetic susceptibility averages 67.3 IU and exhibits high-amplitude variability ranging between 25 and 174 IU. It should be noted that the absolute values of the magnetic susceptibility measurements at Site U1477 may be bi-

Figure F16. *P*-wave velocity, bulk density (black line = WRMSL measurements, red circles = MAD measurements), magnetic susceptibility (black line = WRMSL measurements, red circles = SHMSL measurements), Hole U1477A.



ased to lower values for some intervals because of voids resulting from significant core expansion.

Compressional wave velocity

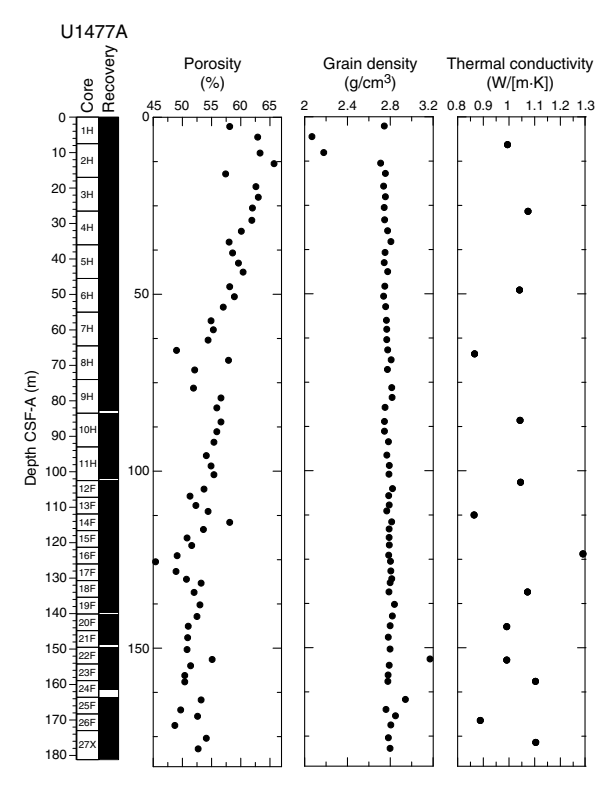
P-wave velocities measured with the WRMSL (Figure **F16**) in Hole U1477A increase with a high gradient from 1520 m/s at the seafloor to 1593 m/s at 2.4 m CSF-A. This increase is followed by a sharp decrease to 1490 m/s at 5.6 m CSF-A. Below 5.6 m CSF-A, velocities exhibit a gradual increase to 1534 m/s at 16.9 m CSF-A. Below this depth, reliable P-wave data collection in all holes of Site U1477 was inhibited by strong signal attenuation caused by the high number of gas expansion voids so no values are included in the figure.

Moisture and density

Bulk density at Site U1477 was determined on whole-core sections using the STMSL and WRMSL (GRA density) and discrete MAD samples. Changes in GRA and MAD bulk densities are well correlated throughout Hole U1477A (Figure **F16**). GRA bulk density values vary from 1.13 to 2 g/cm³ and are consistent with an average MAD bulk density of 1.81 \pm 0.1 g/cm³. Spike-like excursions to lower GRA bulk densities (e.g., at 64 m CSF-A) may be due to voids caused by gas expansion and the generally slightly higher values for discrete samples are likely also explained by the gas expansion voids. Grain densities vary between 2.10 and 3.17 g/cm³ with an average value of 2.77 \pm 0.1 g/cm³ (Figure **F17**).

Overall, the porosity profile (Figure **F17**) shows a decreasing downhole trend in Hole U1477A that is consistent with sediment compaction. Porosity values are low compared to Sites U1474–U1476, and range between 45.4% and 65.7%.

Figure F17. Porosity, grain density, and thermal conductivity, Hole U1477A.



Thermal conductivity

Thermal conductivity measurements were performed on every other core in Holes U1477A and U1477B (Figure F17). The full-space needle probe was used, usually near the middle of one section. Overall, thermal conductivity values range between 0.86 and 1.29 W/(m·K), with an average value of 1.03 W/(m·K), but do not show an increase with depth as observed at previous sites.

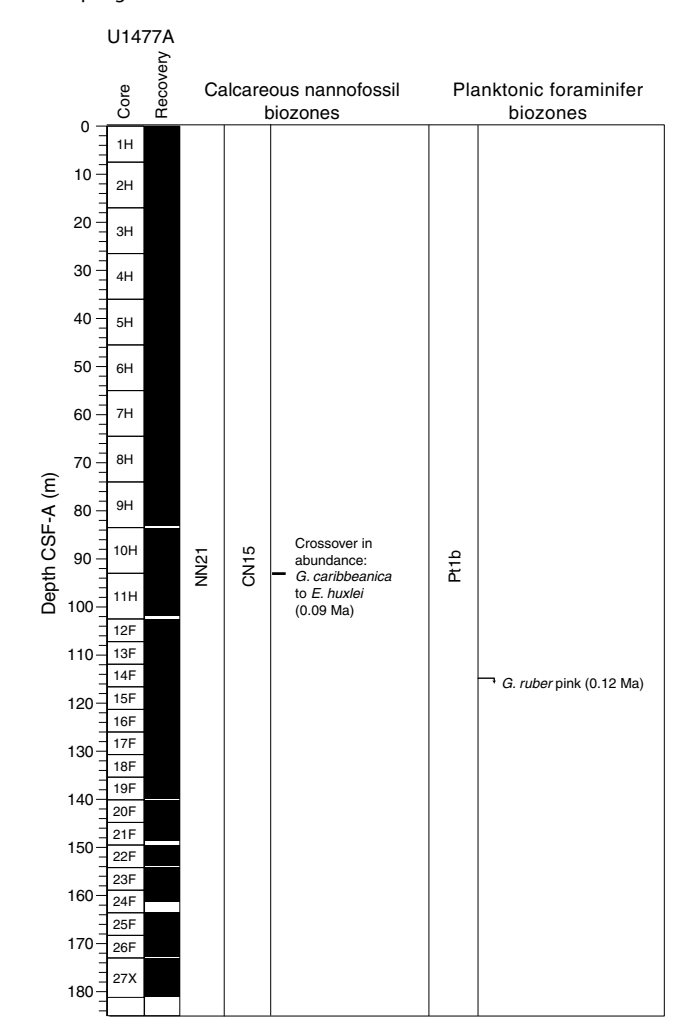
Summary

Despite the homogeneous lithology, different physical parameters at Site U1477 show complex patterns of high-amplitude changes that are likely caused by climate-related variations in terrigenous sediment supply or current sorting effects. However, some spike-like excursions to lower values in NGR and GRA density data may be due to voids caused by gas expansion. Also, reliable *P*-wave data collection below 16.9 m CSF-A in all holes at Site U1477 was inhibited by strong signal attenuation caused by the frequent occurrence of gas expansion voids. The porosity profile at Site U1477 shows a decreasing trend downhole, and average porosities are significantly lower when compared to the sites (U1474–U1476 and U1479) in deeper water, suggesting a higher degree of sediment compaction.

Micropaleontology

Site U1477 spans approximately the last 200 ky of the Pleistocene. Analysis of calcareous nannofossils and planktonic foraminifers identifies two biostratigraphic datums—the abundance crossover of the nannofossils *Gephyrocapsa caribbeanica* to *Emiliania huxleyi* at ~90 ka and the top occurrence of planktonic foraminifer *Globigerinoides ruber* (pink) at ~120 ka. Diatoms were too

Figure F18. Biochronology at Site U1477 with significant planktonic foraminifer and calcareous nannofossil events. Biochronology is based exclusively on sampling in Hole U1477A.



sparse to yield a biostratigraphy. Calcareous nannofossils are generally well preserved in the clay-rich Hole U1477A, although abundance is typically low. Planktonic foraminifers are <1% of sediment particles in most samples, whereas calcareous nannofossils show abundances of <50 liths per field of view throughout the hole. The planktonic assemblage, which includes the regular occurrence of pteropods, is joined by benthic foraminifers, ostracods, sponge and gorgonian spicules, phytoliths, mollusks, echinoderm plates, and fish otoliths. Because of the high sedimentation rates (estimated as 1 m/ky) at this site, only core catcher samples were fully examined, for a total of 26 samples, with just a few additional samples examined from the split cores.

The biostratigraphy of Hole U1477A is shown in Figure F18 with microfossil datums reported in Tables T4 and T5. Calcareous nannofossil occurrences are presented in Table T6, and planktonic foraminifer occurrences are shown in Table T7. Typical examples of calcareous nannofossils at Site U1477 are presented in Figure F19. Representative species of planktonic and benthic foraminifers at Site U1477 are shown in Figure F20, and some examples of assemblages are illustrated in Figure F21. The age-depth plot including the biochronology and magnetostratigraphic datums is discussed in Age model and is shown in Figure F36.

Table T4. Biostratigraphic planktonic foraminifer datums, Site U1477. Quality scores indicate the degree of reliability for each datum based on distinct taxonomy, abundance, and occurrence of the event. 1 = 80% reliability, 2 = 50% - 80% reliability, 3 = 50% reliability. 4 = 50% reliability, 4 = 50% reliability. 4 = 50% reliability, 4 = 50% reliability. 4 = 50% reliability.

Subzone Hole, core, section		Depth CSF-A (m)	Event	Age (Ma)	Quality score
Pt1b	361- U1477A-14H-CC	116.86	T G. ruber (pink)	0.12	1

Table T5. Biostratigraphic calcareous nannofossil datums, Site U1477. Quality score indicates the degree of reliability for the datum based on distinct taxonomy, abundance, and occurrence of the event. 1 = >80% reliability. X = crossover. **Download table in .csv format.**

Bioz	zone/Subzone		Depth		Age	Quality
(Martini, 1971)	ini, 1971) (Okada and Bukry, 1980)		CSF-A (m)	Event	(Ma)	score
		361-U1477A-				
NN21	CN15b	10H-CC	93.02	X G. caribbeanica to E. huxleyi	0.09	1

Table T6. Calcareous nannofossil occurrence, Site U1477. **Download table in .csv format.**

Table T7. Planktonic foraminifer occurrence and abundance based on examination of the >150 μ m fraction, Site U1477. **Download table in .csv format.**

Calcareous nannofossils

Calcareous nannofossils were analyzed in the mudline, 26 core catcher samples, and three selected intervals from the split-core sections in Hole U1477A. Group and individual abundances of discrete species were recorded from the core catcher and split-core section samples. Only one nannofossil datum event calibrated by Gradstein et al. (2012), the crossover in abundance of *G. caribbeanica* to *E. huxleyi* (~0.09 Ma) in Sample 361-U1477A-10H-CC (93.02 m CSF-A), was identified at Site U1477.

Relatively low abundances (<5% of sediment particles) were recorded in the upper part of the sequence (from the mudline to Sample 6H-CC; 55.68 m CSF-A). Abundances slightly increase in Sample 7H-CC (65.28 m CSF-A), reaching their maximum (>50% of sediment particles) in Samples 12F-CC (107.45 m CSF-A) and 13F-CC (111.85 m CSF-A). Between 116.95 and 126.08 m CSF-A (>0.12 Ma based on planktonic foraminifer datums), calcareous nannofossils are still quite common; however, they substantially decrease in abundance (<1% of sediment particles) between Samples 17F-CC (130.97 m CSF-A) and 22F-CC (153.79 m CSF-A). The species that characterize this interval are Florisphaera profunda, Gephyrocapsa oceanica, and small Gephyrocapsa spp. (<4 μm), which are valuable indicators of the nutricline depth (Flores et al., 2000). Finally, from Sample 23F-CC (159.29 m CSF-A) to the bottom of the hole at 180.96 m CSF-A, calcareous nannofossil abundances increase to between 5% and 50% of sediment particles.

Overall, the assemblages are characterized by relatively low species diversity and are dominated by cosmopolitan forms, such as *E. huxleyi*, *G. oceanica*, and small *Gephyrocapsa* (<4 µm) as well as by *F. profunda* and *Gladiolithus flabellatus*, two lower photic zone taxa. Rare to few specimens of *Calcidiscus leptoporus*, *Helicosphaera carteri*, *Syracosphaera pulchra*, small *Reticulofenestra* (<3 µm), *Umbellosphaera irregularis*, *Umbellosphaera tenuis*, and *Umbilicosphaera sibogae* are recorded in the samples. Rare occurrences of *Helicosphaera hyalina*, *Helicosphaera wallichii*, *Pontosphaera japonica*, *Pontosphaera discopora*, *Rhabdosphaera clavigera*, *Discosphaera clavigera*, *Discosphaera discopora*, *Rhabdosphaera clavigera*, *Discosphaera cl*

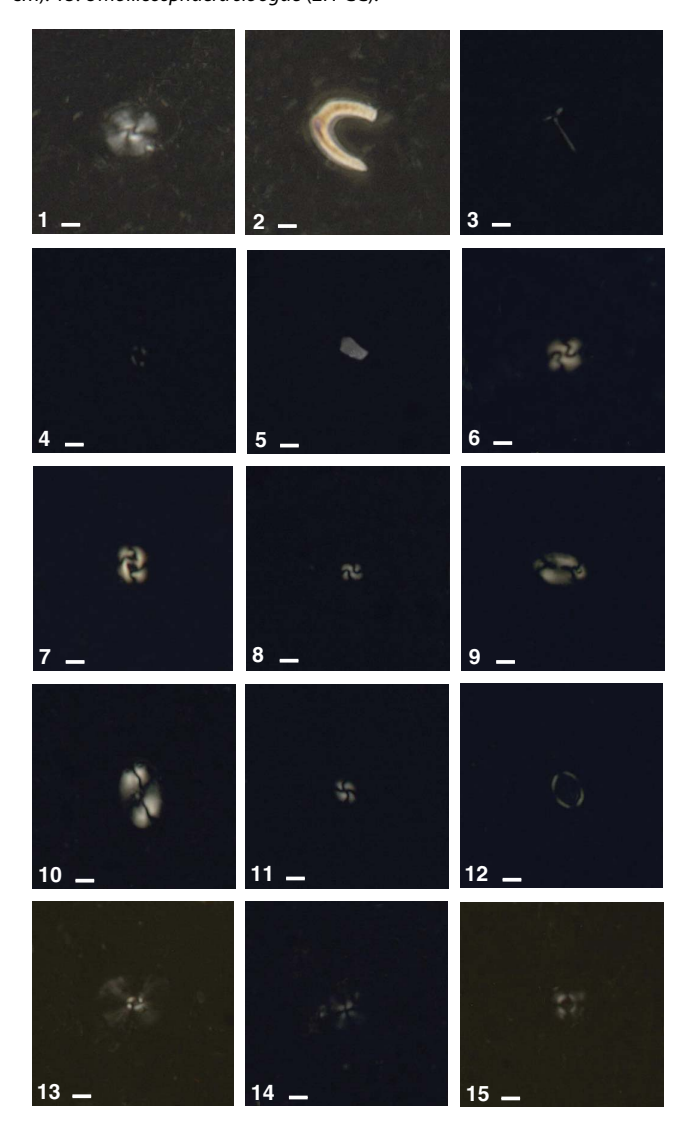
phaera tubifera, Calsiosolenia murrayi, and Ceratolithus cristatus are also observed.

Planktonic foraminifers

Planktonic foraminifers were examined in core catcher samples in Hole U1477A and one core catcher sample in Hole U1477B for a total of 27 samples. Most samples were washed directly upon core recovery, a task that became increasingly difficult because of the compacted clay in the deeper parts of the hole. The core catchers from Cores 361-U1477A-24F (161.3 m CSF-A) through 27X (180.9 m CSF-A) and 361-U1477B-26F (174.8 m CSF-A) were dried completely before processing and soaked in a dilute borax solution—a procedure that made the samples much easier to process and likely resulted in an improvement in foraminifer quality in the washed sand fraction. Examples of the major foraminifer taxa present at Site U1477 are illustrated in Figures F20 and F21. Foraminifer residues (>63 μ m) typically constitute from <<1% to ~1% of the total sediment volume, with the highest abundance reached in Samples 361-U1477A-12F-CC (107.4 m CSF-A) and 13F-CC (111.8 m CSF-A). Foraminifer preservation is usually excellent, with the typical occurrence of semi-glassy, translucent specimens with empty chambers. However, some intervals also display moderate to poor preservation, commonly from infilling by pyrite, pyrite replacement, and extensive staining with iron oxides. Preservation in sand layers is particularly poor, with iron-stained foraminifers and benthic species (such as Ammonia falsobeccarii) transported in from shallower water.

The planktonic foraminifer assemblage is relatively invariant and is dominated by tropical Indian Ocean species such as G. ruber (white), Globigerinoides sacculifer, Globorotalia menardii, Neogloboquadrina dutertrei, and Globigerinella siphonifera. Globorotalia crassaformis, Orbulina universa, and Pulleniatina obliquiloculata are other typical elements, whereas Globigerinita glutinata, Globigerina bulloides, Globigerinella calida, Globigerinoides conglobatus, and Globorotalia tumida are rare but regularly occurring components. Species with more occasional occurrences include Globorotalia inflata, Neogloboquadrina pachyderma (dextral), Globorotalia hirsuta, Globigerinella obesa, Globigerina falconensis, and Globorotaloides hexagona. Finally, our single biostratigraphically useful species, G. ruber (pink), has its top occurrence in Samples 14F-CC (116.9 m CSF-A), positioning this sample at ~0.12 Ma. G. ruber (pink) was also found in Sample 361-U1477B-13F-CC (111.86 m CSF-A).

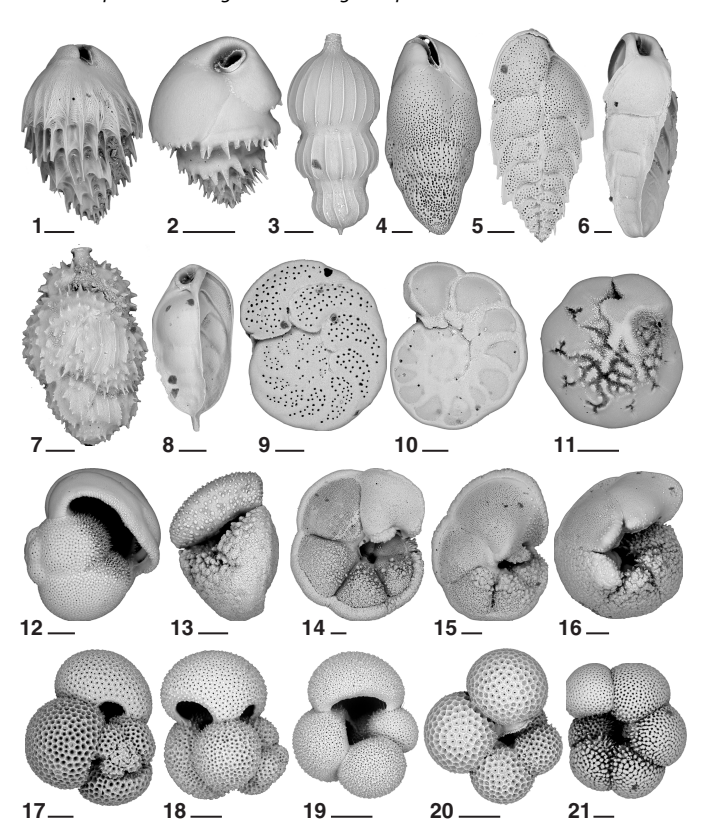
Figure F19. Calcareous nannofossils, Hole U1477A. Scale bars = 2 μ m. 1. *Calcidiscus leptoporus* (13F-CC). 2. *Ceratolithus cristatus* (13F-CC). 3. *Discosphaera tubifera* (14F-2, 120 cm). 4. *Emiliania huxleyi* (14F-2, 120 cm). 5. *Florisphaera profunda* (14F-2, 120 cm). 6. *Gephyrocapsa caribbeanica* (13F-CC). 7. *Gephyrocapsa oceanica* (2H-CC). 8. Small *Gephyrocapsa* (14F-2, 120 cm). 9. *Helicosphaera carteri* (2H-CC). 10. *Helicosphaera* sp. (13F-2, 65 cm). 11. Small *Reticulofenestra* (14F-2, 120 cm). 12. *Syracosphaera* sp. (2H-CC). 13. *Umbellosphaera irregularis* (2H-CC). 14. *Umbellosphaera tenuis* (13F-2, 65 cm). 15. *Umbilicosphaera sibogae* (2H-CC).



Siliceous microfossils

Diatoms, silicoflagellates, phytoliths, and sponge spicules make up a minor component of Hole U1477A samples and exhibit poor preservation in core catcher samples (Table T8). The mudline sample has moderate preservation and a mixed assemblage of marine, littoral, and freshwater diatoms. Other siliceous microfossils present in the mudline sample are phytoliths and sponge spicules. Ma-

Figure F20. Benthic and planktonic foraminifers, Hole U1477A. Scale bars = 100 µm. Images 1–11 are from Sample 5H-CC; images 12–21 are from Sample 12H-CC. 1. Bulimina striata. 2. Bulimina marginata. 3. Amphicoryna scalaris. 4. Bulimina subornata. 5. Brizalina alata. 6. Bolivinita quadrilatera. 7. Uvigerina bradyana. 8. Bolivinita quadrilatera. 9. Planulina (Cibicidoides) wuellerstorfi. 10. Hyalinea balthica. 11. Ammonia falsobeccarii. 12. Pulleniatina obliquiloculata. 13. Globorotalia crassaformis. 14. Globorotalia menardii. 15. Globorotalia tumida. 16. Globorotalia truncatulinoides (sinistral). 17. Globigerinoides sacculifer. 18. Globigerinoides ruber. 19. Globigerina bulloides. 20. Globoquadrina hexagona. 21. Neogloboquadrina dutertrei.



rine diatoms represented in the mudline are taxa such as *Azpeitia* spp., *Paralia sulcata, Triceratium favus*, and *Rhizosolenia bergonii*. Also present are littoral taxa such as *Cocconeis* spp., *Diploneis bombus*, and *Navicula* spp. Terrestrial inputs are represented by the freshwater diatom, *Aulacoseira* spp., and other freshwater diatom fragments, along with the presence of phytoliths.

Core catcher samples contain trace amounts of siliceous microfossils that exhibit poor preservation. Several core catcher samples are barren of diatoms (Table T8); however, other siliceous microfossils such as sponge spicules and phytoliths are consistently present downcore. Marine diatoms were found along with indicators of terrestrial inputs in Samples 361-U1477A-10H-CC (93.07 m CSF-A), 11H-CC (101.88 m CSF-A), and 24F-CC (161.39 m CSF-A); however, the primary siliceous microfossil signal at this site is from sponge spicules, phytoliths, and littoral and freshwater diatoms. Datums for tropical diatoms were not observed at this site due to the high sedimentation rate.

Figure F21. A–F. Representative assemblages of foraminifers and other sedimentary components, Site U1477. In particular, note the (B) pyritized burrow fillings; (C) coarse mollusk, bryozoan, and coral skeletal debris; (D) agglutinated benthic foraminifers, mollusks, and a fish otolith; and (F) pyritized sediment with pyritized foraminifers. Scale bars = $200 \mu m$.

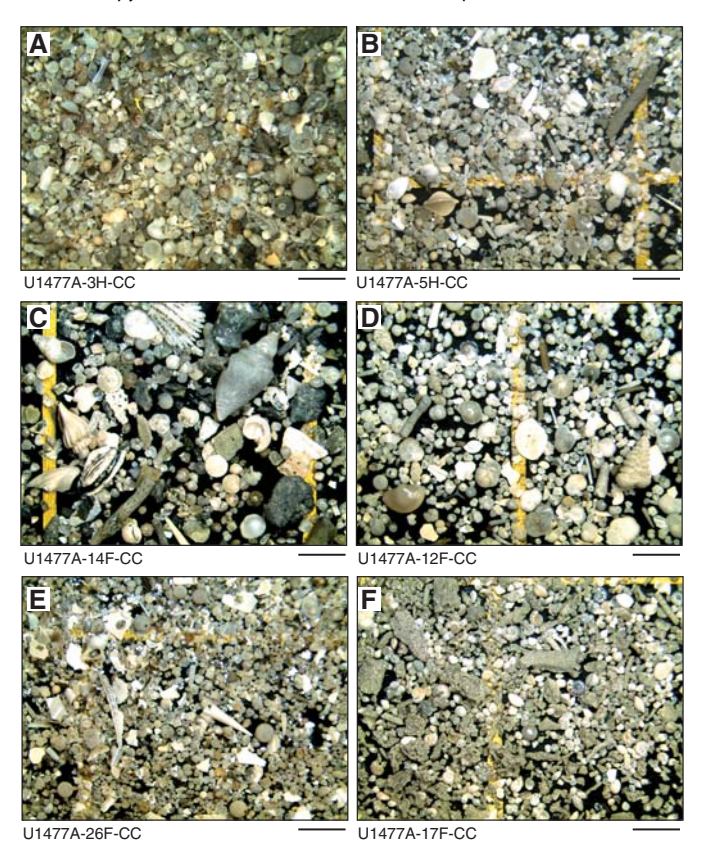


Table T8. Diatom and other siliceous microfossil occurrences, Site U1477. **Download table in .csv format.**

Paleomagnetism

For Site U1477, sediment cores were recovered from Holes U1477A, U1477B, and U1477C with maximum penetration of 181.2, 174.4, and 119.4 m CSF-A, respectively. The Icefield MI-5 core orientation tool was used to measure orientations of sediment cores from Hole U1477A. However, this tool failed and the FlexIt tool was used for APC cores in Holes U1477B (Cores 1H through 12H) and U1477C (Cores 2H through 10H). Discrete samples were taken from Holes U1477A and U1477C for natural remanent magnetization (NRM) demagnetization, anisotropy of magnetic susceptibility (AMS), and isothermal remanent magnetization (IRM) acquisition experiments.

Discrete sample measurements

Bulk magnetic susceptibility reaches the highest values of ~600 \times 10⁻⁶ SI at ~5 and ~10 m CSF-A in Holes U1477A and U1477C, respectively. Below it tends to vary between 100 and 250 \times 10⁻⁶ SI with a maximum value of 500 \times 10⁻⁶ SI between 130 and 140 m CSF-A. Trends in the volumetric magnetic susceptibility obtained from discrete samples aligns with the SHMSL magnetic susceptibility data (Figure **F22**; Table **T9**).

Figure F22. (A) S-ratio, (B) HIRM, (C) SIRM, and (D) magnetic susceptibility, Holes U1477A and U1477C.

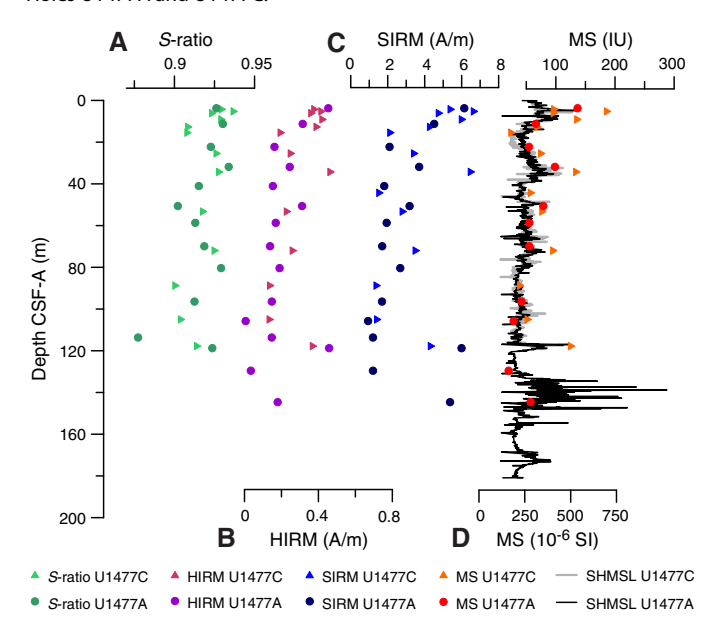


Table T9. Volumetric bulk magnetic susceptibility and declination of maximum magnetic susceptibility eigenvalues of discrete samples, Site U1477. **Download table in .csv format.**

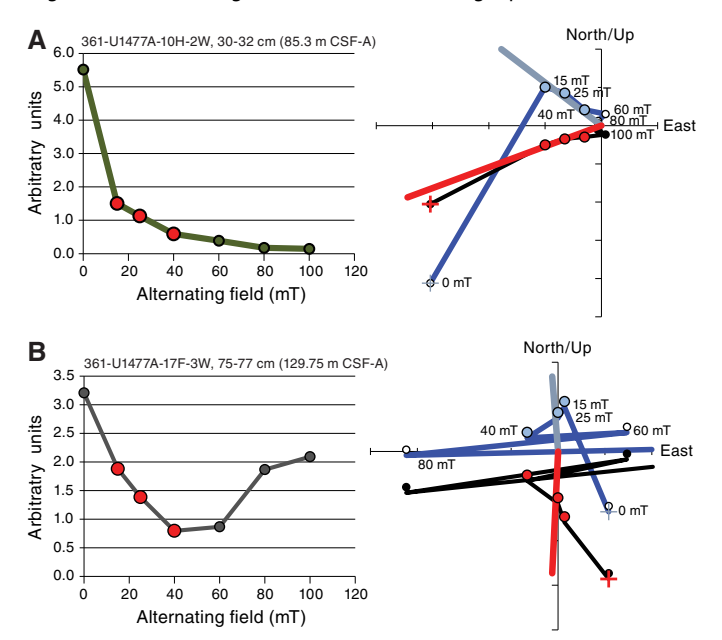
Table T10. Analyzed discrete whole-round samples, Site U1477. **Download table in .csv format.**

Because the Icefield MI-5 tool failed to work correctly in Hole U1477A, directional data could not be corrected for the orientation of cores retrieved in this hole; subsequent investigations found that the Icefield MI-5 tool had not operated correctly since Site U1476. However, the orientation angle that was obtained by the FlexIt tool was successfully applied to correct the directional data in Hole U1477B except for Core 361-U1477B-3H. The declinations of the eigenvalues of the maximum magnetic susceptibility (V₁) were corrected for core orientation considering a modal declination of 0° for each of these cores (Table T10). Because of the relatively high magnetic susceptibility of the sediments at this site, the shipboard AMS data might be less affected by magnetic noise of the shipboard surroundings and therefore provide information on the magnetic fabric of the sediment related to the current direction at the time of sediment deposition. These preliminary AMS results indicate that the magnetic minerals are aligned in northern and southeastern directions (Table T9). These directions are consistent with currentinduced sediment transport pathways from the Zambezi River and along the Mozambique margin.

Saturation IRM (SIRM) decreases from ~ 5 to ~ 1 A/m at ~ 16 m CSF-A (Figure F22). Further downcore, SIRM is relatively stable with a few elevated values coinciding with magnetic susceptibility peaks. Hard IRM (HIRM) shows the same trend as SIRM. S-ratios vary between 0.9 and 0.93, and the lowest values are generally associated with relatively low magnetic susceptibility.

Upon demagnetization of NRM most of the samples show stable directions (Figure $\mathbf{F23A}$). However, Sample 361-U1477A-17F-3, 75–77 cm, from 129.75 m CSF-A shows acquisition of magnetization at right angles to the last demagnetization axes (arbitrary order

Figure F23. A, B. Alternating field (AF) demagnetization results from two samples from Hole U1477A. Left panels show the loss in NRM upon progressive demagnetization, right panels show orthogonal projections of the demagnetization paths. Black (white) symbols mark the projections on the horizontal (vertical) plane. Red and blue circles indicate which demagnetization steps were used for PCA. Sample in B shows the acquisition of gyroremanent magnetization during AF treatment at fields >40 mT at right angles to the last demagnetization direction (see right panel).



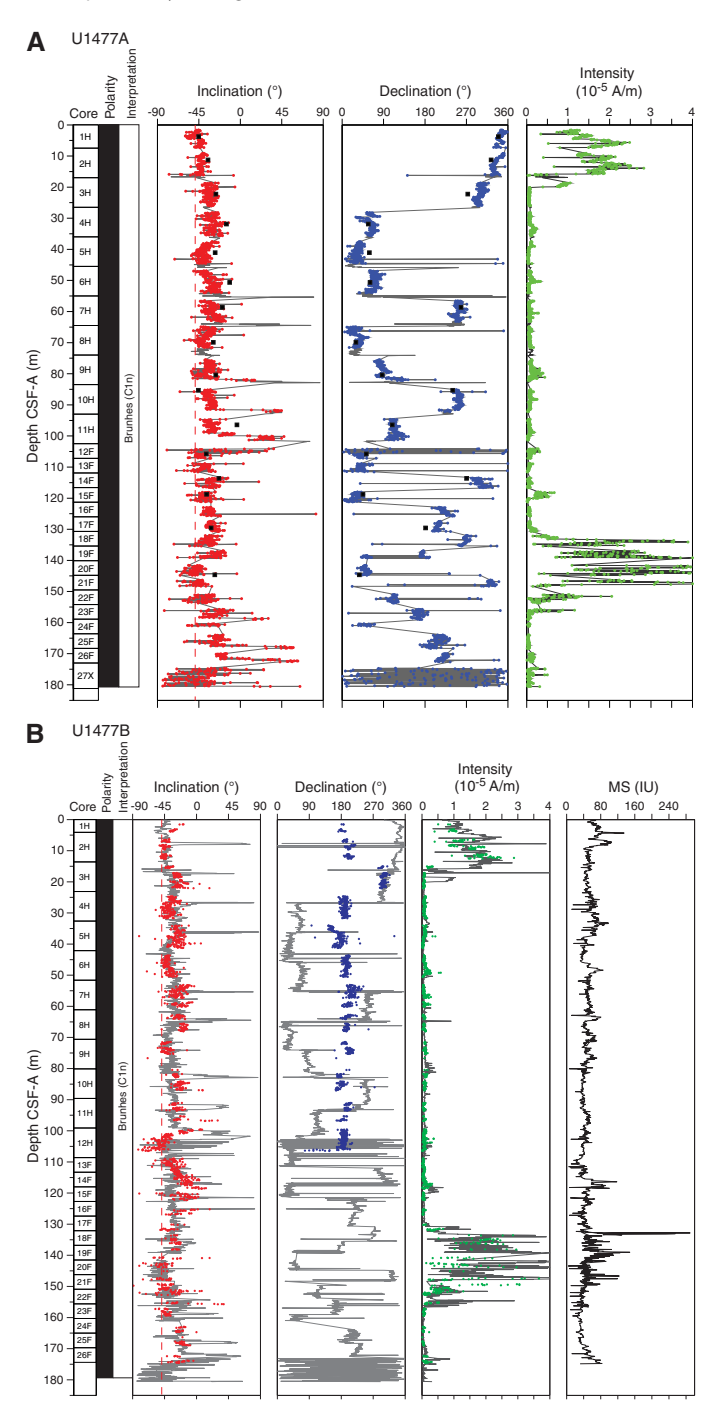
of x, y, and z demagnetization axes) after the 40, 60, and 80 mT step (Figure **F23B**). This so-called gyroremanent magnetization is typical for the presence of greigite. The current sulfate—methane transition zone (SMTZ) was observed at ~16 m CSF-A (see **Geochemistry**). Sedimentary records from the Zambezi margin suggest that the SMTZ remains at approximately the same depth horizon as a result of the decrease in sediment accumulation rates after the flooding of the Mozambique shelf (März et al., 2008). This suggests that ample time is available in these sediments for associated early diagenetic processes, as dissolution and iron-sulfide (e.g., greigite) formation to overprint the magnetic mineralogy.

Inclinations before demagnetization show steep downward (\sim 80°) inclinations, as are typically observed for core drill string overprint. Characteristic remanent magnetizations were computed by performing principal component analyses (PCA) on incremental demagnetization steps, with median angular deviations <18°. All discrete samples show inclinations that are characteristic for normal polarity.

Archive-half measurements

Results from Core 361-U1477A-1H, which was demagnetized at 15, 20, and 25 mT, indicate that for most of the sections the coring overprint was successfully removed after the highest demagnetization step. Therefore, the remaining cores from Holes U1477A and U1477B as well as Cores 361-U1477C-2H through 6H were demagnetized at 25 mT, and inclinations average ~50° (Figure F24). Drilling disturbances and overprints have a notable effect on the inclination and declination data from the first and last section of each core. Additionally, inclination and declination data from sections that were retrieved by HLAPC are much noisier than those retrieved by APC.

Figure F24. Downhole inclination, declination, and intensity after demagnetization at 25 mT, Site U1477. Sediment with normal polarity that can be assigned to the Brunhes Chron. Gray lines = data, vertical dashed line = present-day inclination, colored circles = data without the last and first sections of each core. Black squares = discrete sample inclination from PCA. A. Hole U1477A. B. Hole U1477B. For visibility, corrected declination data (blue circles) is plotted by adding 180°.



Magnetostratigraphy

All recovered cores have inclinations of ~50°, similar to present-day inclination at Site U1477. No reversed intervals occur in the downhole inclination records, indicating that the sediments exclusively cover a part of the Brunhes normal polarity chron.

Stratigraphic correlation

Three holes were drilled at Site U1477 using the APC, HLAPC, and XCB systems and contain a reasonably complete section covering the last glacial cycle at extremely high resolution. Exceptionally high accumulation rates (~1 m/ky; see Age model) and accompanying high rates of organic carbon accumulation result in a high gas (CH₄) content and consequently significant expansion of the cores upon decompression. This produced intervals of severe fracturing with many voids and substantial extension of individual core lengths. The nature of the sediment also led to relatively early refusal of the full-length APC barrel at ~80-90 m DSF (see Operations). This resulted in partial recovery of material and suspected flow-in of material in some cores around this depth in all holes (see Sedimentology). Furthermore, significant and apparently real differences between holes (reflected by various parameters including magnetic susceptibility, reflectance, and NGR compared on a meter scale) implies that construction of a continuous splice for the full length of the record is not possible and would be effectively meaningless, at least for the interval below ~85 m CCSF-A. Consequently, a continuous splice has been constructed only for the upper 85 m CCSF-A, with the deeper interval (downhole to ~195 m CCSF-A) being represented almost exclusively by Hole U1477B, which we consider the highest quality material. However, this choice, even for the uppermost 85 m CCSF-A, must be taken as subjective. Future investigations should consider differences between holes as potentially real and of possible significance to the broader inferences made from this site.

Irrespective of any real differences among holes on a meter scale, which prevents direct correlation across several intervals, there is clear correlation of several parameters across all three holes on a scale of 5–10 m, even on the CSF-A scale (Figure F25). This gives us confidence that the sediment at this site reflects representative environmental variations and can be used to make inferences about wider regional processes.

Compositing of holes

As a guide for drilling to avoid coring gap alignment where possible, sequences from all holes were composited in near-real-time using magnetic susceptibility data from the STMSL (see **Physical**

properties in the Expedition 361 methods chapter [Hall et al., 2017] for details) measured at 5 cm resolution. After collection, compositing of holes was achieved using the whole-round magnetic susceptibility measurements almost exclusively—in this case from the STMSL—but results from the WRMSL were effectively identical and could have been used instead. Magnetic susceptibility was the preferred variable for stratigraphic ties because the gas expansion and fracturing led to especially noisy signals in other records (e.g., NGR and color reflectance). The relative depth offset of each core was determined by the optimized correlation of the magnetic susceptibility record (Figure F26), with the top of Hole U1477B serving as the mudline anchor. These depth offsets are reported in the affine Table T11.

Where a lack of distinct features prevented straightforward correlation between holes (notably below ~85 m CCSF-A) or where distinct differences between holes made correlation impossible, offsets (gaps) between cores were estimated by extrapolation of the growth factor from the core above. Typically this was ~10%, with some modest variation of this average growth rate to accommodate the few stratigraphic ties that could be made confidently (e.g., near the base of the recovered section).

Construction of the splice

Once the composite depth scale was created, select sequences from Holes U1477A–U1477C were spliced together to create a complete section downhole to \sim 85 m CCSF-A (Figure F27). Below this depth it was not possible to construct a continuous sequence, and distinct differences among holes (possibly exacerbated by problems associated with refusal of the APC) renders the exercise potentially meaningless. Consequently, the interval between \sim 85 and 195 m CCSF-A is represented in the splice almost exclusively by material from Hole U1477B (Table T12). Although it is not possible to precisely determine the width of gaps between cores within this interval, they have been estimated by assuming a relatively constant growth rate of \sim 10% throughout this section.

Again, it should be stressed that any future study of material from this site needs to consider the differences among holes as potentially valuable illustrations of regional processes. Our particular choice of cores within all parts of the splice does not necessarily reflect the most representative of that interval.

Figure F25. Magnetic susceptibility records on the CSF-A depth scale, Site U1477. Scale applies to all offset data from individual holes.

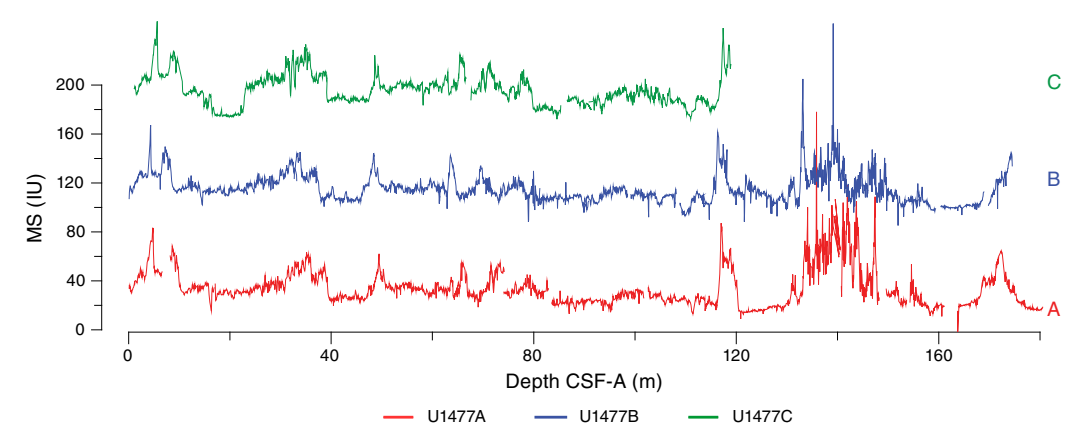


Figure F26. Magnetic susceptibility records on the CCSF-A depth scale, Site U1477. Scale applies to all offset data from individual holes.

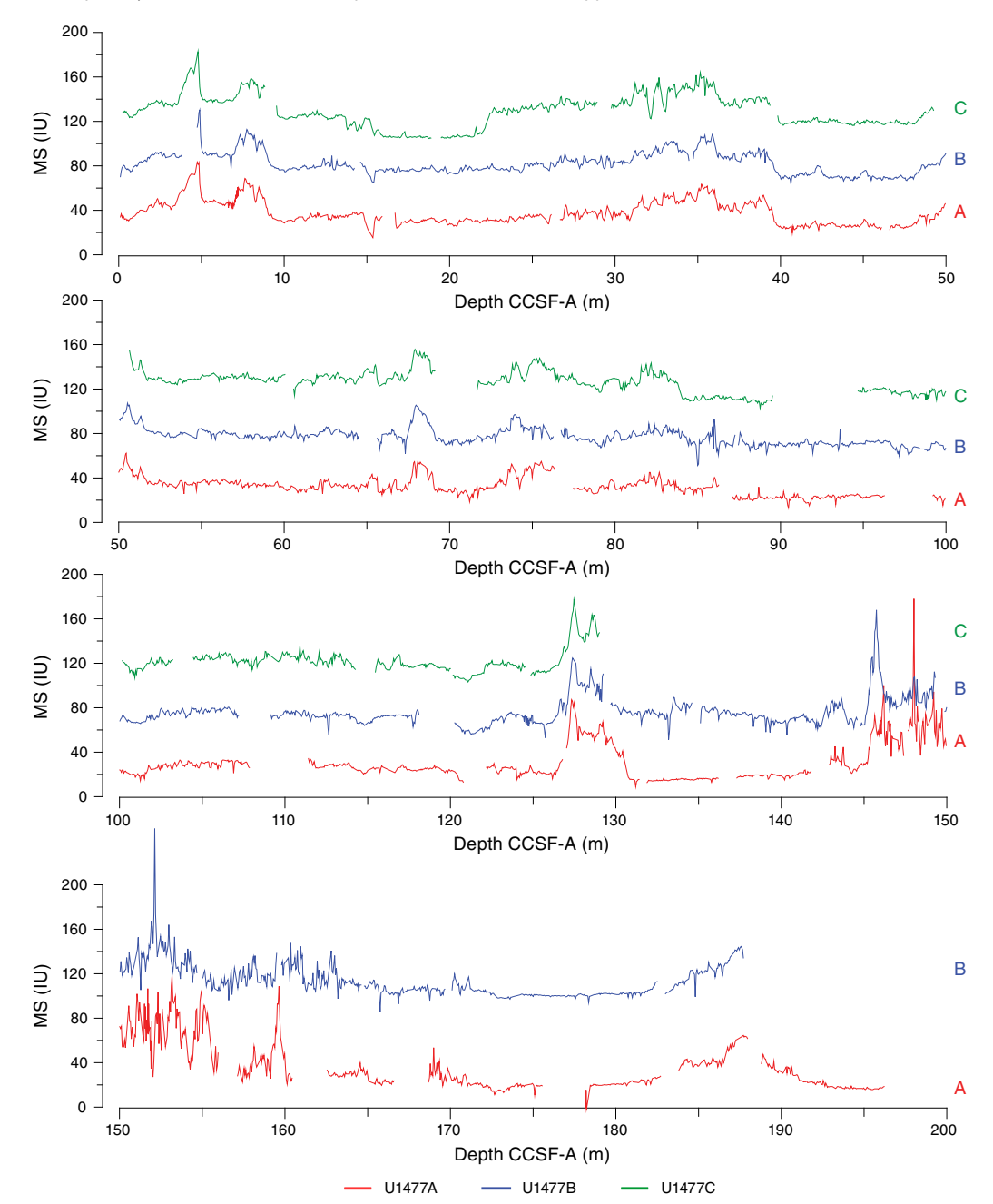


Table T11. Affine table, Site U1477. Download table in .csv format.

Figure F27. Composite spliced records of magnetic susceptibility and NGR, Site U1477. Dashed vertical line = bottom of the continuous splice as described in text.

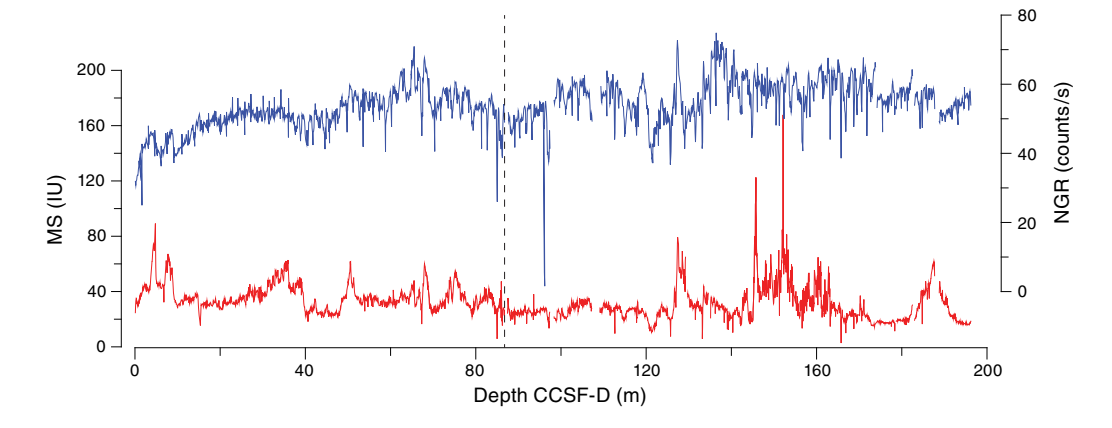


Table T12. Splice interval table, Site U1477. Download table in .csv format.

Geochemistry

The chemical composition of headspace gases, interstitial waters, and bulk sediments were investigated at Site U1477. Sampling for shipboard analyses focused in Hole U1477A. Downhole profiles of interstitial water chemistry largely reflect postdepositional microbially mediated reactions driven by the rapid accumulation of organic carbon. Sedimentary carbonate contents range from 1 to 22 wt%, with an average of 5.5 wt%. Interstitial water profiles of redox-sensitive species indicate more intense diagenesis at this site than all the other sites, with anoxic conditions near the top of the core and complete sulfate reduction by ~16 m CSF-A (Figure F28).

Interstitial water was squeezed from 5 and 10 cm whole rounds at \sim 3 m resolution from 2.95 to 26.06 m CSF-A and \sim 9.5 m resolution between 24.06 and 172.03 m CSF-A in Hole U1477A. A total of 25 samples were collected from Hole U1477A for shipboard analysis of interstitial water chemistry. Bulk sediment in Hole U1477A was measured for total organic carbon (TOC) and total inorganic carbon (TIC) content in samples selected as representative of the lithology.

Sedimentary hydrocarbon gases

Headspace gas samples were collected from each core in Hole U1477A. A total of 20 samples were measured, with the uppermost 3 samples measured the following day because of instrument difficulties in the initial run. In all samples, ${\rm CH_4}$ is the primary hydrocarbon present, and only trace levels of ethene, ethane, and propene were detected. Methane concentrations increased from 29 ppmv at 6.0 m CSF-A to ~75,500 ppmv at 35.75 CSF-A in Core 361-U1477A-4H and then decreased for the remainder of the sampled cores (Figure **F28**). This is likely the result of bacterial methanogenesis (Barnes and Goldberg, 1976). Below ~100 m CSF-A, methane concentrations remain below ~10,000 ppmv.

Interstitial water chemistry

Salinity, chloride, sodium, magnesium, and potassium

Salinity, chloride, and sodium are relatively constant and near or slightly elevated above average seawater values in all samples from Hole U1477A (Figure **F29**). Average values ($\pm 1\sigma$) are 552.7 \pm 3.6 mM chloride and 467.8 \pm 8.8 mM sodium. The downhole chloride profile displays a minor increase in the upper ~ 50 m CSF-A followed by a slight decrease further downhole. Magnesium and po-

Figure F28. Concentration profiles that highlight microbial-driven reactions and redox cycling in the upper 80 m CSF-A, Hole U1477A.

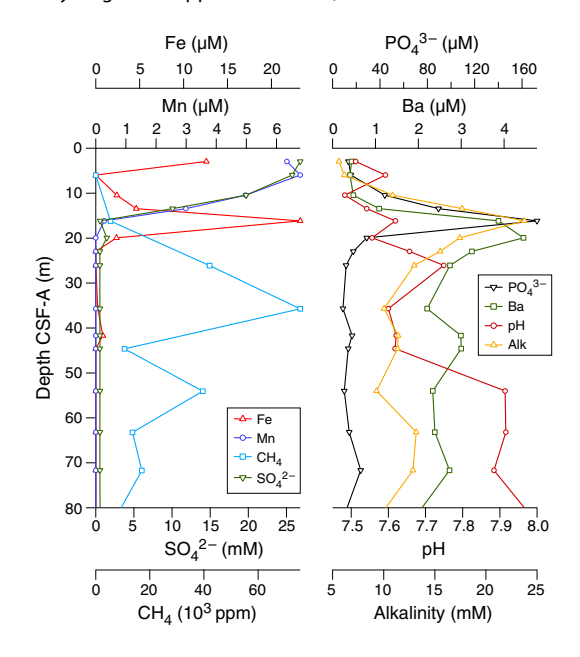
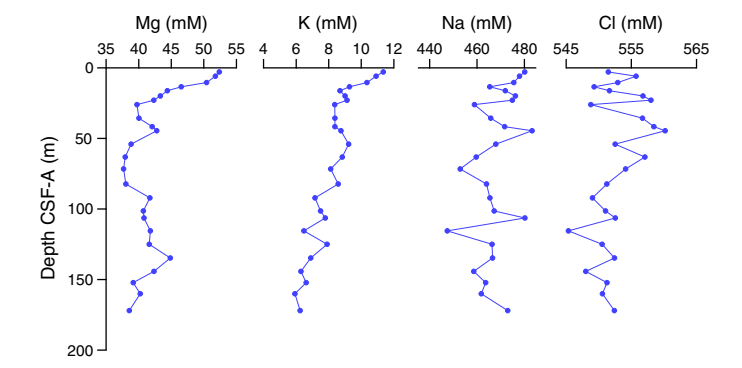


Figure F29. Dissolved magnesium, potassium, sodium, and chloride profiles, Hole U1477A.



tassium concentrations decrease downhole from maximum values of 52.4 mM Mg and 11.3 mM K at 2.95 m CSF-A to minima of 37.7 mM Mg and 5.9 mM K near the bottom of Hole U1477A. The downhole potassium profile displays a monotonic decrease in con-

centration, whereas the magnesium profile displays more variability. The $\sim\!50\%$ drawdown of potassium between the mudline and the bottom of Hole U1477A suggests significant uptake of potassium by clay minerals at depth.

Alkalinity, phosphate, and pH

Alkalinity is 5.6 mM at 2.95 m CSF-A, increases to a maximum of 23.8 mM at 16.16 m CSF-A, and remains relatively stable below ~26 m CSF-A with an average of 12.4 \pm 2.0 mM in Hole U1477A (Figure F30). The downhole phosphate profile resembles the alkalinity profile, with concentrations increasing sharply from 13.4 μM at 2.95 m CSF-A to 172.6 μM at 16.16 m CSF-A and a relatively stable concentration of 15.3 \pm 5.2 μM below ~26 m CSF-A. pH increases downhole from ~7.5 at 2.95 m CSF-A to ~8 at 82.24 m CSF-A and averages 7.83 \pm 0.10 below ~54 m CSF-A.

Iron and manganese

In Hole U1477A, the concentration of dissolved iron is 12.6 μ M at 2.95 m CSF-A and decreases downhole except for an abrupt increase to 23.3 μ M at 16.16 m CSF-A, which coincides with peaks in the downhole profiles of alkalinity and phosphate (Figures **F28**, **F31**). Below ~23 m CSF-A, the concentration of dissolved iron remains below the detection limit. Analytical issues with the iron standard calibration make it difficult to interpret measured values below 4.5 μ M. However, the initial sample at 2.95 m CSF-A and two points that make up the maximum at 16.16 m CSF-A are within the calibrated range. The downhole dissolved manganese profile dis-

Figure F30. Alkalinity, dissolved phosphate, and pH profiles, Hole U1477A.

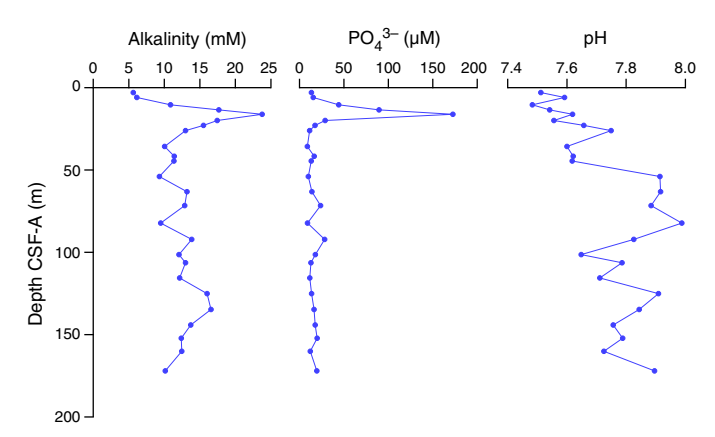
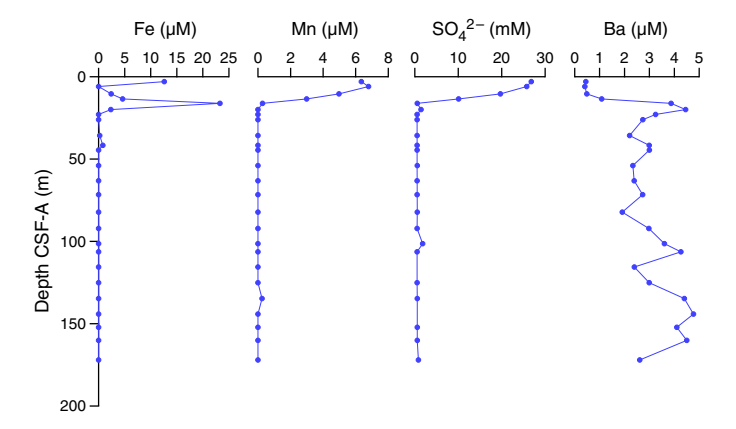


Figure F31. Dissolved iron, manganese, sulfate, and barium, Hole U1477A. Samples with values below the detection limit are plotted as zeros.



plays maximum concentrations 6.4 μ M in the uppermost two samples at 2.95 m CSF-A and 6.8 μ M at 5.95 m CSF-A before decreasing monotonically to below the detection limit at 19.95 m CSF-A. Decreasing dissolved manganese concentrations below the zone of dissolution in the uppermost ~6 m likely reflects its combination with HCO₃⁻ and formation of manganese carbonate minerals (Calvert and Pedersen, 1994). The downhole dissolved iron profile likely indicates that reductive dissolution of iron oxides is occurring around 16.16 m CSF-A and that precipitation of iron sulfide minerals removes the dissolved iron as it diffuses away from the zone of active reductive dissolution.

Sulfate and barium

Sulfate concentrations in Hole U1477A decrease rapidly downhole from a near-seawater concentration of 26.8 mM at 2.95 m CSF-A to below the detection limit at 16.16 m CSF-A (Figures F28, F31). This is likely the result of microbial sulfate reduction, in which sulfate is used as an electron receptor in the anaerobic oxidation of organic matter:

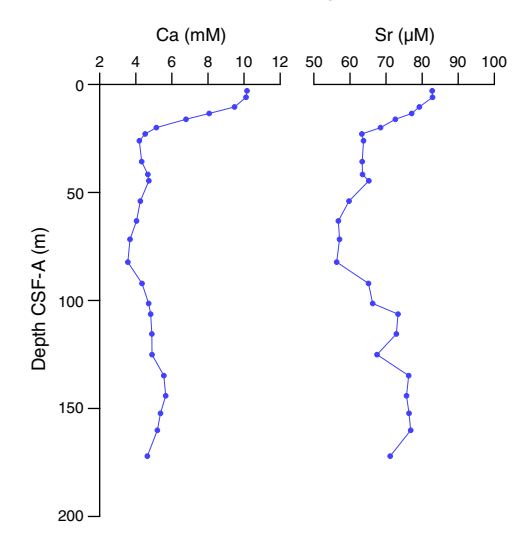
$$53 \text{ SO}_4^{2-} + (\text{CH}_2\text{O})_{106}(\text{NH}_3)_{16}(\text{H}_3\text{PO}_4) \rightarrow 39 \text{ CO}_2 + 67 \text{ HCO}_3^- + 16 \text{ NH}_4^+ + 53 \text{ HS}^- + 39 \text{ H}_2\text{O} + \text{HPO}_4^{2-}.$$

At this site, the disappearance of sulfate in interstitial water coincides with the sharp increase in methane. This is the sulfate—methane transition zone and indicates that there is more microbial activity at this site than at previous sites, likely due to the significantly higher organic carbon accumulation rates. In sediment where sulfate reduction is rapid and intense, barite (BaSO₄) will dissolve. In Hole U1477A, barium increases from minimum concentrations of <0.5 μM in the upper 10.45 m CSF-A to between ~2 and 5 μM below 16.16 m CSF-A, which is coincident with the abrupt decrease in sulfate. This indicates dissolution of barite.

Calcium and strontium

Concentrations of calcium in interstitial water in Hole U1477A rapidly decrease from a maximum of 10.2 mM at 2.95 m CSF-A to values around 4 mM at ~25m CSF-A before decreasing to a minimum of 3.6 mM at 82.24 m CSF-A. Calcium concentrations then show a slight increase to the bottom of the section (Figure F32). The downhole strontium profile roughly follows the pattern observed for calcium, with the highest concentration of 82.8 μ M at 2.95 m

Figure F32. Dissolved calcium and strontium profiles, Hole U1477A.



CSF-A followed by decreasing concentrations to a minimum value of $56.3~\mu M$ at 82.24~m CSF-A and slightly increasing concentrations to the bottom of the section.

Silicon, lithium, and boron

The downhole silicon profile in Hole U1477A displays increasing concentrations from 363.2 μ M at 2.95 m CSF-A to a maximum concentration of 750.0 μ M at 16.16 m CSF-A, which coincides with peaks in the downhole profiles of alkalinity, phosphate, and iron (Figure **F33**). Below 16.16 m CSF-A, silicon concentrations vary between 164.2 and 669.4 μ M.

The downhole lithium profile in Hole U1477A varies significantly. Lithium concentrations decrease with depth from 18.5 μM in the uppermost sample at 2.95 m CSF-A to a minimum concentration of 3.1 μM at 152.20 m CSF-A. The decreasing trend is interrupted by a broad peak with a maximum lithium concentration of 19.7 μM at 125.05 m CSF-A. Another peak occurs at the base of the section. Boron concentrations are noisy but decrease from >480 μM in the upper 10.45 m CSF-A to a minimum of 208.7 μM at 152.2 m CSF-A.

Bulk sediment geochemistry

Total organic carbon

Total organic carbon varies from 0.2 to 1.1 wt% with an average of 0.61 wt% for all samples measured (Figure F34). No systematic

Figure F33. Dissolved silicon, lithium, and boron profiles, Hole U1477A.

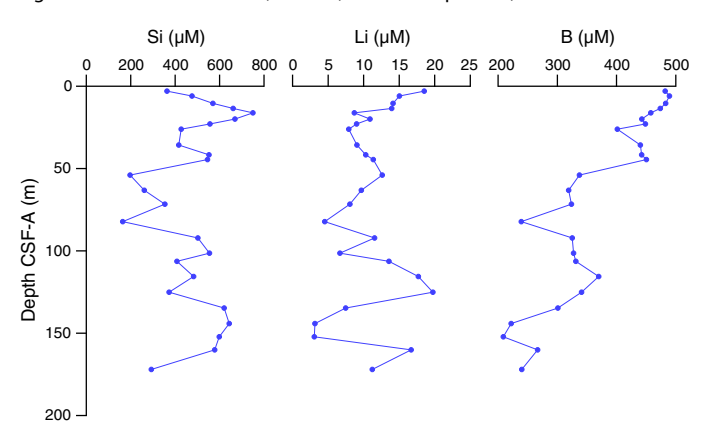
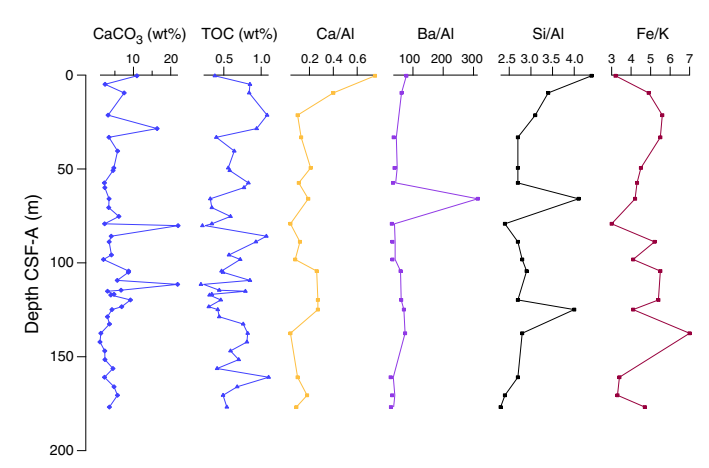


Figure F34. Calcium carbonate, TOC, and bulk sediment elemental ratios, Hole U1477A.



pattern relating organic carbon and carbonate or other lithologic properties such as magnetic susceptibility was observed.

Calcium carbonate

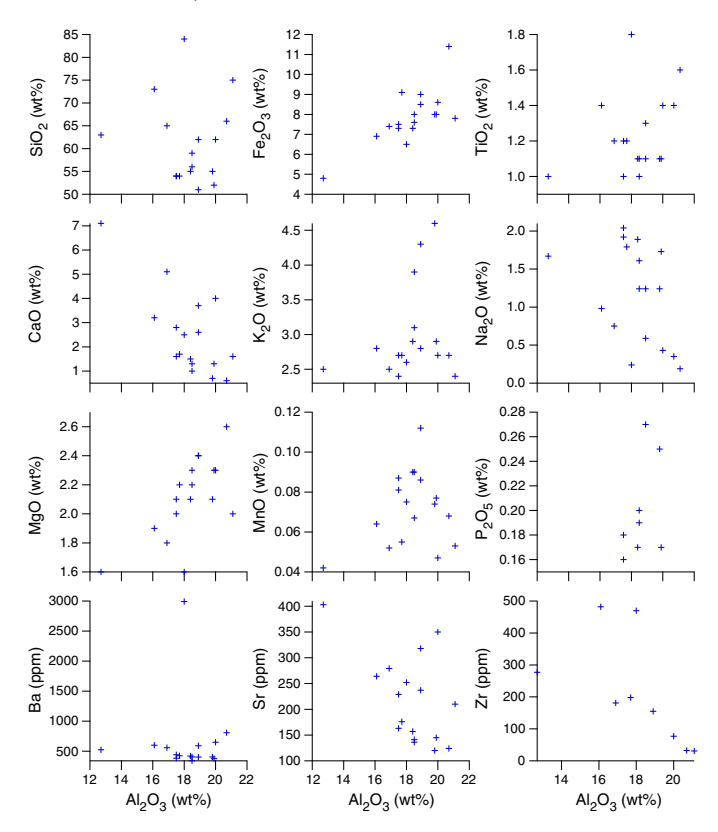
Calcium carbonate contents range between 1 and 22 wt% with an average of 5.5 wt% at Site U1477 (Figure F34). Carbonate contents remain low for most of the core, with large spikes likely caused by preferential sampling of carbonate-rich shell-bearing intervals. No significant trend in carbonate content was observed at Site U1477.

Major and trace elements

Major and trace element concentrations were measured for 17 samples taken for calcium carbonate analyses from Hole U1477A (Table T13). Bulk sediment data for Site U1477 are in stark contrast to the previous sites, where biogenic calcium carbonate is a dominant sedimentary component. Bulk sediment concentrations of Al, Ti, and Fe are greater than those of average upper continental crust, whereas Ca, Sr, and Na concentrations are below average crustal values (Taylor and McLennan, 1985). Few elements show any significant correlation with aluminum oxide contents (Figure F35). Calcium oxide does display an inverse relationship with aluminum, and the low CaO concentrations imply that all or most of the calcium is present within carbonate minerals. Iron and magnesium oxides display weak positive correlations with aluminum oxide. This is almost certainly due to the extremely high abundance of biotite mica at this site (see Sedimentology). The abundant mica may also explain the

Table T13. Shipboard bulk sediment geochemistry data, Hole U1477A. **Download table in .csv format.**

Figure F35. Sedimentary major and trace element concentrations vs. aluminum oxide content, Hole U1477A.



average crustal K_2O values in spite of the extremely low concentrations of CaO and Na_2O . It is possible that Ca and Na were lost over many cycles of chemical weathering, whereas K was concentrated in the mica that was subsequently deposited at Site U1477. In addition, the abundance of platy mica significantly reduces porosity (see **Physical properties**), leaving little space for interstitial water and essentially removing Na contamination from dried pore fluid.

Downhole profiles of elemental ratios at Site U1477 reflect the dominance of lithogenic sediment (Figure F34). Ca/Al values are extremely low, with a maximum value of 0.75 in the uppermost sample (361-U1477A-1H-1, 40-41 cm). Below ~10 m CSF-A, Ca/Al values are even lower (0.15 ± 0.08) and generally follow carbonate content. Ba/Al values are also low and invariable with the exception of one outlier at 65.89 m CSF-A (Sample 8H-2, 113-114 cm). The Si/Al profile is also relatively flat with the exception of a decrease in the upper ~30 m CSF-A and two outliers at 65.89 and 124.88 m CSF-A. The decrease in Si/Al values in the upper 30 m CSF-A is also present in K/Al, Mg/Al, and Sr/Al profiles (not shown), coinciding with an increase in Fe/K and implying a change in sediment provenance or transport over this time interval. Below ~30 m CSF-A, there is variability in Fe/K values that is not present in Si/Al values and may indicate varying degrees of chemical weathering in the Zambezi Catchment.

Redox processes

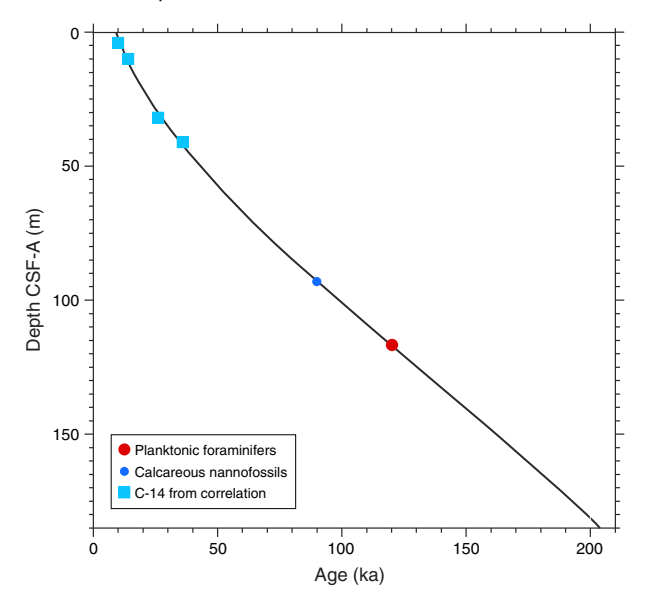
The rapid accumulation of terrigenous sediment resulted in significant dilution of biogenic carbonate and high rates of microbial respiration at Site U1477. The resulting interstitial water and headspace gas concentrations show the consumption of oxidized species, including iron and manganese oxides and sulfate, and the production of methane during methanogenesis (Figure F28). The abrupt sulfate—methane transition at ~16 m CSF-A shows the immediate consumption of upward-diffusing methane in the presence of sulfate. This depth interval is marked by peaks in alkalinity and phosphate, two by-products of high rates of respiration, and peaks and barite and iron related to enhanced dissolution of barite and iron bearing minerals.

Age model

A total of 181 m of Late Pleistocene to Holocene sediment was recovered from Hole U1477A. The age model is based on the biochronology of calcareous nannofossils and planktonic foraminifers along with the correlation to the radiocarbon-dated age models of nearby piston Cores 64PE304-80 and GIK16160-3 (van der Lubbe et al., 2014) over the past 20 ky. These correlations were made based on the distinctive magnetic susceptibility profiles of all cores. Biostratigraphic sampling at Site U1477 included 27 core catcher samples from Hole U1477A. We report biostratigraphic events in Tables T4 and T5, and major age-depth trends are illustrated in Figure F36

The age-depth model provides an estimate of \sim 0.2 Ma for the basal age of Site U1477. The correlation of the Site U1477 MS profile to the radiocarbon-dated age models of nearby piston cores suggests that sedimentation rates were greatest between \sim 30 and 40 ka (\sim 30 m CSF-A in Hole U1477A) to the present (\sim 1.5 m/ky), with slower rates (or even a hiatus) at the top of the record. The long-term average sedimentation rate before \sim 0.05–0.06 Ma (\sim 50 m CSF-A in Hole U1477A) is \sim 83 cm/ky but is estimated by only two biostratigraphic datums. A third-order polynomial fit has an r^2 = 0.999 and extrapolates to a bottom age in Sample 361-U1477A-27X-CC (181 m CSF-A) of \sim 0.2 Ma.

Figure F36. Age-depth relationships for Site U1477. Radiocarbon calibrations come from nearby piston Cores 64PE304-80 and GIK16160-3 (van der Lubbe et al., 2014) that have been transferred to the Site U1477 record through correlation of the Site U1477 magnetostratigraphy records with these dated records. Additional points come from the *G. caribbeanica/E. hux-leyi* crossover (~90 ka) and the last occurrence of *G. ruber* (pink) (~120 ka). Regression line is a third-order polynomial fit to all data and suggests a ~1.5 m/ky sedimentation rate shallower than ~30 m CSF-A and a ~83 cm/ky sedimentation rate deeper than ~50 m CSF-A.



References

Barnes, R.O., and Goldberg, E.D., 1976. Methane production and consumption in anoxic marine sediments. *Geology*, 4(5):297–300. http://dx.doi.org/10.1130/0091-7613(1976)4<297:MPA-CIA>2.0.CO;2

Beiersdorf, H., Kudrass, H.R., and von Stackelberg, U., 1980. Placer deposits of ilmenite and zircon on the Zambezi shelf. *Geologisches Jahrbuch, Reihe D: Mineralogie, Petrographie, Geochemie, Lagerstaettenkunde*, 36:5–85.

Calvert, S.E., and Pedersen, T.F., 1994. Sedimentary geochemistry of manganese; implications for the environment of formation of manganiferous black shales. *Economic Geology*, 91(1):36–47. http://dx.doi.org/10.2113/gsecongeo.91.1.36

Dupont, L.M., Caley, T., Kim, J.-H., Castañeda, I., Malaizé, B., and Giraudeau, J., 2011. Glacial–interglacial vegetation dynamics in south eastern Africa coupled to sea surface temperature variations in the Western Indian Ocean. Climate of the Past, 7(4):1209–1224.

http://dx.doi.org/10.5194/cp-7-1209-2011

Dupont, L.M., Donner, B., Vidal, L., Pérez, E.M., and Wefer, G., 2005. Linking desert evolution and coastal upwelling: Pliocene climate change in Namibia. Geology, 33(6):461–464. http://dx.doi.org/10.1130/G21401.1

Euroconsult Mott MacDonald, 2008. Integrated Water Resources Management Strategy and Implementation Plan for the Zambezi River Basin: Lusaka, Zambia (SADC-WD/Zambezi River Authority).

 $\label{lem:http://www.zambezicommission.org/downloads/Zambezi River\\ Basin IWRM Strategy ZAMSTRAT.pdf$

Flores, J.-A., Bárcena, M.A., and Sierro, F.J., 2000. Ocean-surface and wind dynamics in the Atlantic Ocean off Northwest Africa during the last 140,000 years. *Palaeogeography, Palaeoclimatology, Palaeoecology*, 161(3–4):459–478. http://dx.doi.org/10.1016/S0031-0182(00)00099-7

Gammelsrød, T., 1992. Variation in shrimp abundance on the Sofala Bank, Mozambique, and its relation to the Zambezi River runoff. *Estuarine, Coastal and Shelf Science*, 35(1):91–103.

http://dx.doi.org/10.1016/S0272-7714(05)80058-7

- Gradstein, F.M., Ogg, J.G., Schmitz, M.D., and Ogg, G.M. (Eds.), 2012. *The Geological Time Scale 2012*: Amsterdam (Elsevier).
- Hall, I.R., Hemming, S.R., LeVay, L.J., Barker, S., Berke, M.A., Brentegani, L., Caley, T., Cartagena-Sierra, A., Charles, C.D., Coenen, J.J., Crespin, J.G., Franzese, A.M., Gruetzner, J., Han, X., Hines, S.K.V., Jimenez Espejo, F.J., Just, J., Koutsodendris, A., Kubota, K., Lathika, N., Norris, R.D., Periera dos Santos, T., Robinson, R., Rolinson, J.M., Simon, M.H., Tangunan, D., van der Lubbe, J.J.L., Yamane, M., and Zhang, H., 2017. Expedition 361 methods. *In* Hall, I.R., Hemming, S.R., LeVay, L.J., and the Expedition 361 Scientists, *South African Climates (Agulhas LGM Density Profile)*. Proceedings of the International Ocean Discovery Program, 361: College Station, TX (International Ocean Discovery Program).
 - http://dx.doi.org/10.14379/iodp.proc.361.102.2017
- Johnson, T.C., Brown, E.T., McManus, J., Barry, S., Barker, P., and Gasse, F., 2002. A high-resolution paleoclimate record spanning the past 25,000 years in southern East Africa. *Science*, 296(5565):113–132. http://dx.doi.org/10.1126/science.1070057
- Just, J., Schefuß, E., Kuhlmann, H., Stuut, J.-B.W., and Pätzold, J., 2014. Climate induced sub-basin source-area shifts of Zambezi River sediments over the past 17 ka. *Palaeogeography, Palaeoclimatology, Palaeoecology*, 410:190–199. http://dx.doi.org/10.1016/j.palaeo.2014.05.045
- Lutjeharms, J.R.E., 2006. *The Agulhas Current:* Berlin (Springer-Verlag). http://dx.doi.org/10.1007/3-540-37212-1
- März, C., Hoffmann, J., Bleil, U., de Lange, G.J., and Kasten, S., 2008. Diagenetic changes of magnetic and geochemical signals by anaerobic methane oxidation in sediments of the Zambezi deep-sea fan (SW Indian Ocean). Marine Geology, 255(3–4):118–130.
 - http://dx.doi.org/10.1016/j.margeo.2008.05.013
- Maslin, M.A., Pancost, R.D., Wilson, K.E., Lewis, J., and Trauth, M.H., 2012. Three and half million year history of moisture availability of south West Africa: evidence from ODP Site 1085 biomarker records. *Palaeogeogra-phy, Palaeoclimatology, Palaeoecology*, 317–318:41–47. http://dx.doi.org/10.1016/j.palaeo.2011.12.009
- Moore, A.E., Cotterill, F.P.D., Main, M.P.L., and Williams, H.B., 2008. The Zambezi River. *In Gupta*, A. (Ed.), *Large Rivers: Geomorphology and Management:* Chichester, United Kingdom (John Wiley & Sons, Ltd.), 311–332. http://dx.doi.org/10.1002/9780470723722.ch15
- Reason, C.J.C., Landman, W., and Tennant, W., 2006. Seasonal to decadal prediction of southern African climate and its links with variability of the Atlantic Ocean. *Bulletin of the American Meteorological Society*, 87(7):941–955. http://dx.doi.org/10.1175/BAMS-87-7-941
- Ronco, P., Fasolato, G., and Di Silvio, G., 2006. The case of the Zambezi River in Mozambique: some investigations on solid transport phenomena downstream Cahora Bassa Dam. *In* Alves, E., Cardoso, A., Leal, J., and

- Ferreira, R. (Eds.), *Proceedings of the International Conference on Fluvial Hydraulogy:* Lisbon, Portugal (Taylor & Francis).
- Schulz, H., Lückge, A., Emeis, K.-C., and Mackensen, A., 2011. Variability of Holocene to Late Pleistocene Zambezi riverine sedimentation at the upper continental slope off Mozambique, 15°–21°S. *Marine Geology*, 286(1–4):21–34. http://dx.doi.org/10.1016/j.margeo.2011.05.003
- Schefuß, E., Kuhlmann, H., Mollenhauer, G., Prange, M., and Pätzold, J., 2011. Forcing of wet phases in southeast Africa over the past 17,000 years. Nature, 480(7378):509–512. http://dx.doi.org/10.1038/nature10685
- Siddorn, J.R., Bowers, D.G., and Hoguane, A.M., 2001. Detecting the Zambezi River Plume using observed optical properties. *Marine Pollution Bulletin*, 42(10):942–950.
 - http://dx.doi.org/10.1016/S0025-326X(01)00053-4
- Taylor, R.S., and McLennan, S.M., 1985. The Continental Crust: Its Composition and Evolution: Oxford, United Kingdom (Blackwell Scientific Publications, Ltd.).
- Trauth, M.H., Larrasoaña, J.C., and Mudelsee, M., 2009. Trends, rhythms and events in Plio–Pleistocene African climate. *Quaternary Science Reviews*, 28(5–6):399–411.
 - http://dx.doi.org/10.1016/j.quascirev.2008.11.003
- van der Lubbe, H.J.L., Frank, M., Tjallingii, R., and Schneider, R.R., 2016. Neodymium isotope constraints on provenance, dispersal, and climate-driven supply of Zambezi sediments along the Mozambique margin during the past ~45,000 years. *Geochemistry, Geophysics, Geosystems*, 17(1):181–198. http://dx.doi.org/10.1002/2015GC006080
- van der Lubbe, H.J.L., Tjallingii, R., Prins, M.A., Brummer, G.-J.A., Jung, S.J.A., Kroon, D., and Schneider, R.R., 2014. Sedimentation patterns off the Zambezi River over the last 20,000 years. *Marine Geology*, 355:189–201. http://dx.doi.org/10.1016/j.margeo.2014.05.012
- Walford, H.L., White, N.J., and Sydow, J.C., 2005. Solid sediment load history of the Zambezi Delta. *Earth and Planetary Science Letters*, 238(1–2):49–63. http://dx.doi.org/10.1016/j.epsl.2005.07.014
- Wang, Y.V., Larsen, T., Leduc, G., Andersen, N., Blanz, T., and Schneider, R.R., 2013. What does leaf wax δD from a mixed C_3/C_4 vegetation region tell us? *Geochimica et Cosmochimica Acta*, 111:128–139. http://dx.doi.org/10.1016/j.gca.2012.10.016
- Weldeab, S., Lea, D.W., Oberhänsli, H., and Schneider, R.R., 2014. Links between southwestern tropical Indian Ocean SST and precipitation over southeastern Africa over the last 17 kyr. *Palaeogeography, Palaeoclima-tology, Palaeoecology*, 410:200–212.
- http://dx.doi.org/10.1016/j.palaeo.2014.06.001
 Weldeab, S., Stuut, J.-B.W., Schneider, R.R., and Siebel, W., 2013. Holocene climate variability in the winter rainfall zone of South Africa. *Climate of the Past*, 9(5):2347–2364. http://dx.doi.org/10.5194/cp-9-2347-2013